ORIGINAL PAPER

Inhibition of longevity regulator PAPP-A modulates tissue homeostasis via restraint of mesenchymal stromal cells

Mary Mohrin[1] | Justin Liu[1] | Jose Zavala-Solorio[1] | Sakshi Bhargava[2] |
John Maxwell Trumble[2] | Alyssa Brito[2] | Dorothy Hu[3] | Daniel Brooks[4] |
Georgios Koukos[1] | Lama Alabdulaaly[3] | Jonathan S. Paw[1] | Kayley Hake[1] |
Ganesh Kolumam[1] | Mary L. Bouxsein[4,5] | Roland Baron[3,5] | Yuliya Kutskova[2] |
Adam Freund[1]

[1]Calico Life Sciences LLC, South San Francisco, CA, USA

[2]AbbVie Inc, Chicago, IL, USA

[3]Harvard School of Dental Medicine, Boston, MA, USA

[4]Center for Advanced Orthopaedic Studies, Beth Israel Deaconess Medical Center, Boston, MA, USA

[5]Harvard Medical School, Boston, MA, USA

Correspondence
Adam Freund, Calico Life Sciences LLC, South San Francisco, CA, USA.
Email: adam@calicolabs.com

Funding information
Calico Life Sciences, LLC

Abstract

Pregnancy-associated plasma protein-A (PAPP-A) is a secreted metalloprotease that increases insulin-like growth factor (IGF) availability by cleaving IGF-binding proteins. Reduced IGF signaling extends longevity in multiple species, and consistent with this, PAPP-A deletion extends lifespan and healthspan; however, the mechanism remains unclear. To clarify PAPP-A's role, we developed a PAPP-A neutralizing antibody and treated adult mice with it. Transcriptomic profiling across tissues showed that anti-PAPP-A reduced IGF signaling and extracellular matrix (ECM) gene expression system wide. The greatest reduction in IGF signaling occurred in the bone marrow, where we found reduced bone, marrow adiposity, and myelopoiesis. These diverse effects led us to search for unifying mechanisms. We identified mesenchymal stromal cells (MSCs) as the source of PAPP-A in bone marrow and primary responders to PAPP-A inhibition. Mice treated with anti-PAPP-A had reduced IGF signaling in MSCs and dramatically decreased MSC number. As MSCs are (1) a major source of ECM and the progenitors of ECM-producing fibroblasts, (2) the originating source of adult bone, (3) regulators of marrow adiposity, and (4) an essential component of the hematopoietic niche, our data suggest that PAPP-A modulates bone marrow homeostasis by potentiating the number and activity of MSCs. We found that MSC-like cells are the major source of PAPP-A in other tissues also, suggesting that reduced MSC-like cell activity drives the system-wide reduction in ECM gene expression due to PAPP-A inhibition. Dysregulated ECM production is associated with aging and drives age-related diseases, and thus, this may be a mechanism by which PAPP-A deficiency enhances longevity.

KEYWORDS
aging, bone marrow, collagen, extracellular matrix, hematopoiesis, insulin/IGF-1 signalling, mesenchymal stem cells

1 | INTRODUCTION

Initially appreciated for its essential role in fetal and postnatal development, the insulin-like growth factor (IGF) signaling pathway has also been implicated in the regulation of aging and lifespan since the discovery that partial loss-of-function mutations in the *C. elegans daf-2* gene, the ortholog of the human insulin and IGF receptors, can double lifespan (Kenyon et al., 1993). This is highly conserved: a reduction in IGF signaling has been found to delay aging and extend lifespan in multiple species, including mammals (Barbieri et al., 2003; Fontana et al., 2010; Kenyon, 2010). Many mutations in the IGF signaling pathway delay aging in mice, but therapies to target IGF signaling for age-related diseases, let alone aging itself, remain absent from the clinic (Junnila et al., 2013). Failed clinical trials of IGF-1 receptor inhibitors for cancer have led some to conclude that this pathway is a therapeutic dead-end, largely due to compensatory endocrine signaling from growth hormone (GH), insulin, and other growth factors (Beckwith & Yee, 2015; Crudden et al., 2015; Gombos et al., 2012).

Pregnancy-associated plasma protein-A (PAPP-A) is a metalloprotease that cleaves IGF-binding proteins (IGFBPs), specifically IGFBP-2, IGFBP-4, and IGFBP-5. This specificity provides a way to tune IGF signaling without affecting the endocrine IGF-1 circuit. When PAPP-A is deleted, circulating levels of GH and IGF-1 do not change, and thus do not elicit compensatory feedback or elevation of GH (Conover & Bale, 2007; Conover et al., 2004). Instead, PAPP-A works within the local IGF circuit: it increases local IGF signaling by cleaving IGFBP-2, IGFBP-4, or IGFBP-5, liberating IGFs to signal through their receptor. Conversely, inhibition of PAPP-A allows IGFBPs to accumulate, sequestering IGFs and reducing local IGF signaling. Although PAPP-A is secreted, it is localized to the cell surface by glycosaminoglycan binding (Laursen et al., 2002), perhaps explaining why its effects are primarily local.

The phenotypes of PAPP-A-deficient mice (PAPP-A KO) highlight the power of tuning IGF signaling in vivo. PAPP-A KO mice are proportional dwarfs, pointing to the role of IGF in growth modulation, and are also long-lived, with a ~ 30% increase in both male longevity and female longevity (Conover & Bale, 2007; Conover et al., 2010). Importantly, inducible deletion of PAPP-A in adulthood (5 months of age) results in a ~ 20% lifespan extension (Bale et al., 2017). This suggests the mechanisms by which PAPP-A modulates longevity can be explored in the adult animal without confounding developmental effects and motivated us to focus on adulthood inhibition in this study. Notably, the effects of PAPP-A inhibition on aging go beyond lifespan extension; PAPP-A inhibition delays progression of age-related pathology in multiple tissues (Conover et al., 2010) and age-related thymic atrophy (Vallejo et al., 2009), reduces fat accumulation on a high-fat diet (Conover et al., 2013; Tanner et al., 2008), reduces atherosclerotic plaque progression and neointima formation (Conover et al., 2016; Harrington et al., 2007; Resch et al., 2006), limits spontaneous tumorigenesis and tumor progression in xenograft models (Becker et al., 2015; Conover et al., 2010; Heitzeneder

et al., 2019; Torres et al., 2019), and slows polycystic kidney disease (Kashyap et al., 2020). However, the mechanisms giving rise to this diverse set of phenotypes, and the cell types affected by PAPP-A inhibition, remain largely unknown. Additionally, despite its importance in the regulation of growth and lifespan, the location and regulation of expression of PAPP-A remains relatively opaque. *Pappa* mRNA has been shown to have ubiquitous, yet low, levels of expression across tissues (Harstad & Conover, 2014), but the specific cell types responsible for PAPP-A expression remain unidentified. Lastly, it is unclear which phenotypes observed in the KO mouse will be phenocopied by adult pharmacological inhibition, a key question in the pursuit of PAPP-A-modulating therapies.

To address these unknowns, we developed a neutralizing antibody against PAPP-A and used it to study the tissue, cellular, and transcriptomic consequences of adult PAPP-A inhibition in mice. We found that PAPP-A is indeed relevant during adulthood and is amenable to pharmacological intervention: Not only did PAPP-A inhibition reduce IGF signaling across multiple tissues and phenocopy the effect of genetic deletion on bone, but it also had previously unknown effects on system-wide ECM gene expression, marrow adiposity, and hematopoiesis. Exploring the mechanism behind these seemingly disparate effects, we identified mesenchymal stromal cells as the primary producers and proximal responders to PAPP-A inhibition in bone marrow. We found that MSCs and MSC-like cells in other human and murine tissues are also major producers of PAPP-A, suggesting these conclusions apply beyond the bone marrow and providing a plausible mechanism for the observed multi-tissue effects on gene expression. Our results identify a new regulator of in vivo MSC homeostasis, expand our understanding of the importance of IGF signaling in adult tissues, and suggest that PAPP-A mediates many of its effects via modulation of MSC number and activity. During aging, ECM deposition and MSC activity is altered, with excessive activity in the context of age-related diseases such as fibrosis (El Agha et al., 2017) and downregulation across multiple tissues in normal aging (de Magalhaes et al., 2009; Schaum et al., 2020; Sprenger et al., 2010), perhaps indicating MSC functional exhaustion. Restraining MSC activity and thereby avoiding these two fates may be the mechanism by which PAPP-A inhibition delays multiple aspects of aging and age-related disease.

2 | RESULTS

2.1 | Characterization of a potent and selective PAPP-A neutralizing antibody suitable for in vivo studies

To enable production of a PAPP-A neutralizing antibody, we began by verifying PAPP-A's biochemical activity. We tested PAPP-A's reported ability to cleave IGFBP-2, IGFBP-4, and IGFBP-5 using recombinant components (Laursen et al., 2001; Lawrence et al.,

1999; Monget et al., 2003). As expected, PAPP-A cleaved all three proteins, and the cleavage of IGFBP-2 and IGFBP-4 was strongly enhanced by the addition of IGF-1, while for IGFBP-5, it was not (Figure S1A). For all subsequent experiments, cleavage of IGFBP-5 was tested in the absence of IGF-1. Also as reported previously, the activity of PAPP-A for each of these substrates varied, being the most active against IGFBP-5 and less active against IGFBP-2 and IGFBP-4 (Figure S1B).

PAPP-A is not commonly thought to have IGF-independent effects, though isolated reports suggest possible IGF-independent mechanisms (Jadlowiec et al., 2005). To explore this, we tested whether PAPP-A alone induced gene expression changes. We used HeLa cells because they express minimal endogenous *PAPPA* or *IGFBP4* compared with cell types that expresses biologically relevant amounts of *PAPPA*, such as IMR-90 fibroblasts (Lawrence et al., 1999) (Figure S1C), and we serum starved the cells to remove any IGF-1 present in serum. Therefore, this was a controlled system in which to study the cellular effects of IGF-1, IGFBP-4, and PAPP-A. Addition of IGF-1 to the media stimulated a robust gene expression response, which was closely recapitulated by the addition of IGF-1 + IGFBP-4 + PAPP-A (Figure S1D). In contrast, neither PAPP-A nor IGFBP-4 alone induced any change in gene expression. Although we cannot rule out IGF-independent effects of PAPP-A in other contexts or cell types, this result is consistent with neither PAPP-A nor IGFBP-4 having biological functions beyond modulating IGF signaling.

Having optimized assays to measure PAPP-A activity, we next developed and characterized a neutralizing antibody against PAPP-A (anti-PAPP-A). We found anti-PAPP-A effectively blocked PAPP-A-mediated cleavage of human and murine IGFBP-4 and IGFBP-2, but not IGFBP-5 (Figure S1E). These results are similar to other published PAPP-A neutralizing antibodies, and likely due to different requirements for cleavage between the IGFBP substrates (Boldt et al., 2004; Laursen et al., 2001; Mikkelsen et al., 2008, 2014; Weyer et al., 2007). Consistent with incomplete neutralization of all substrates, we found that anti-PAPP-A bound a C-terminal portion of human, mouse, and rat PAPP-A (aa1213-1627), rather than the active site (Figure S1F) (Mikkelsen et al., 2008). Anti-PAPP-A had sub-nanomolar affinity to murine PAPP-A, with a dissociation constant (K_D) of 61 pM. Anti-PAPP-A had a half maximum inhibitory concentration (IC_{50}) of 1.7 nM for mIGFBP-4 and 0.85 nM for mIGFBP-2 (Figure S1G). To assess whether anti-PAPP-A blocked IGF signaling, we measured phosphorylation of AKT in HEK293T cells upon stimulation with IGF-1 in the presence of IGFBP-4 and PAPP-A. As expected, anti-PAPP-A blocked the signaling downstream of IGF-1 in a dose-dependent fashion (Figure S1H, S1I). In vivo pharmacokinetic studies showed that anti-PAPP-A, formatted as an IgG_1 isotype, has a half-life of 6.42 days in C57BL/6 mice (Figure S1J), allowing for weekly dosing. In summary, we generated a PAPP-A neutralizing antibody with excellent potency, selectivity, and pharmacokinetic properties, allowing us to investigate the effects of pharmacologic PAPP-A inhibition in vivo.

2.2 | PAPP-A inhibition reduces extracellular matrix gene expression and IGF signaling in multiple tissues

PAPP-A KO mice have delayed age-related pathology (Conover et al., 2010), though the mechanism behind this remains unknown. To better understand the effects of adult PAPP-A inhibition, we treated male and female C57BL/6 mice with anti-PAPP-A or an isotype control antibody for 4 months, between 6 and 10 months of age, then analyzed a variety of tissues by RNA-seq. We used 5–6 males and 5–6 females per treatment group and analyzed 9 tissues from each animal (Figure 1A), for a total of 198 RNA-seq libraries, representing, to our knowledge, the most thorough interrogation of local IGF inhibition conducted to date.

Pappa transcript was detectable in all tissues; the lowest expression was found in the liver and highest expression in the skin and kidney (Figure S2A). There was no discernible correlation between the expression pattern of *Pappa*, its substrates (*Igfbp2*, *Igfbp4*, *Igfbp5*), or *Igf1* or *Igf1r* across tissues in control animals (Figure S2B). To identify processes that might explain the systemic effects of PAPP-A on aging, we performed differential expression analysis to identify genes that were affected by anti-PAPP-A similarly across all tissues, in both sexes. This stringent approach yielded two genes that were differentially expressed at a 5% false discovery rate: *Igfbp5* and *Col3a1*, both of which were decreased (Figure 1B). *Igfbp5* acts as a transcriptional readout of IGF signaling: It is downregulated upon IGF inhibition and upregulated upon IGF stimulation in multiple cell types and tissues (Duan et al., 1996; Fleming et al., 2005; Harrington et al., 2007; Kuemmerle, 2000; Resch et al., 2006; Swindell et al., 2010; Ye & D'Ercole, 1998), likely as a negative feedback mechanism. The multi-tissue decrease in *Igfbp5* expression by anti-PAPP-A demonstrates that multiple tissues rely on PAPP-A to regulate local IGF signaling. To rule out the possibility that this finding was driven by a minority of tissues or a single sex, we examined each tissue and sex individually and found that *Igfbp5* trended toward decreased expression in multiple tissues in both males and females (Figure S2C), demonstrating an organism-wide reduction in IGF signaling in response to PAPP-A inhibition.

To identify patterns of differential expression in response to anti-PAPP-A, we performed gene ontology (GO) analysis of the 88 genes with a treatment p-value <0.01 across both sexes and all tissues (Raudvere et al., 2019). This demonstrated that the statistically significant reduction *Col3a1* was only one component of a more coordinated downregulation of ECM-related genes: many of the significantly enriched (adj $p < 0.05$) GO terms in this set of 88 genes related to ECM, of which "collagen-containing extracellular matrix" was the most significant (adj $p = 8.5e-29$, 29 out of the 88 genes we examined by GO analysis were part of this gene set) (Figure 1C, S2D). This gene set consists of 334 genes, and visual inspection of these genes in the multi-tissue volcano plot showed a general decrease in gene expression across the entire set (Figure 1D), demonstrating that the enrichment score above was not an artifact of p-value cutoff. Further, this was not
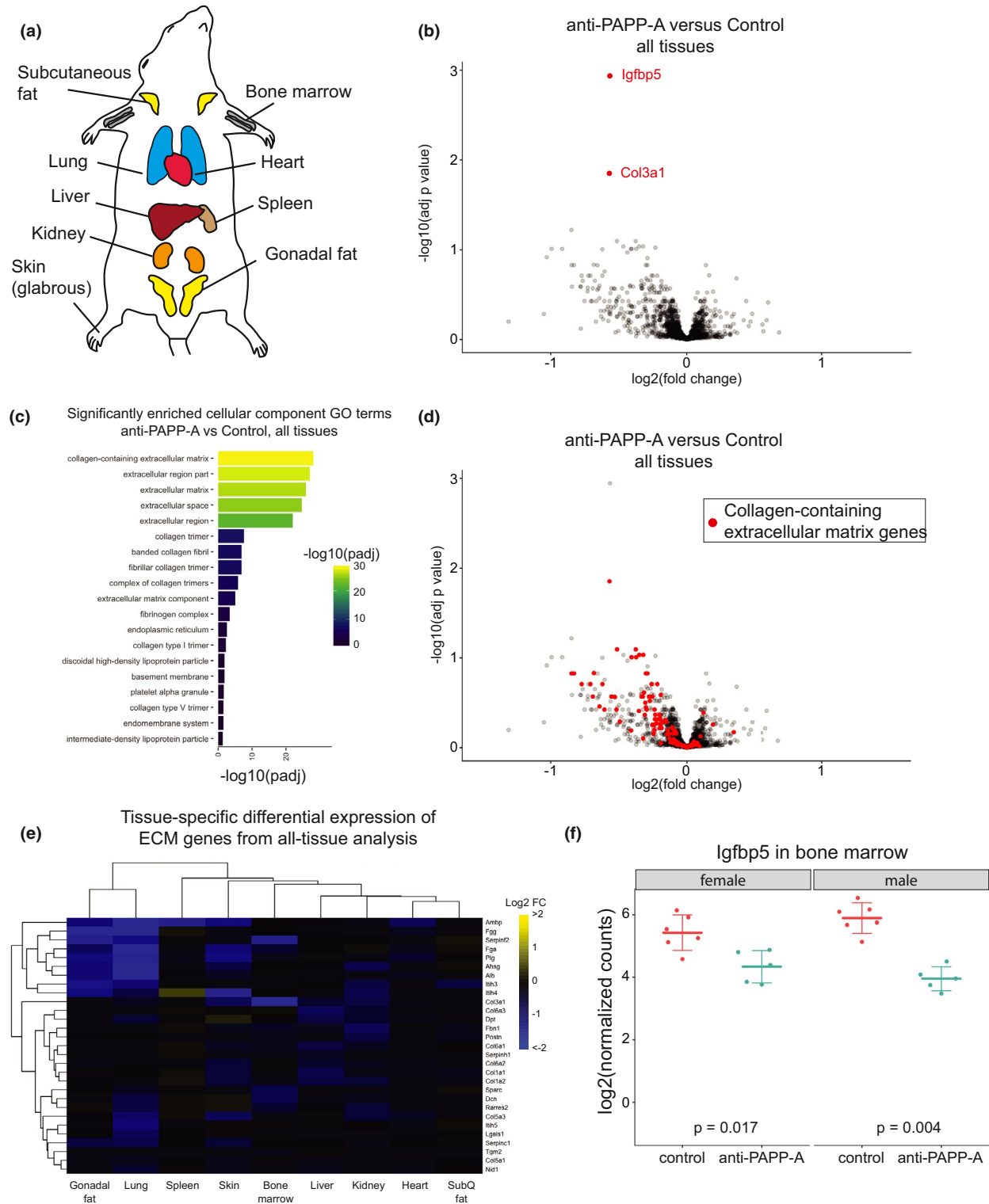
FIGURE 1 PAPP-A inhibition reduces extracellular matrix gene expression and IGF signaling in multiple tissues. (a) Diagram of the nine tissues (lung, liver, kidney, glabrous skin, gonadal fat, subcutaneous fat, spleen, heart, bone marrow) that were isolated and analyzed by RNA-seq from each animal, after 4 months of dosing. n = 6 male and 6 female for control antibody, 5 female and 5 male for anti-PAPP-A (198 total samples). (b) Differential expression due to anti-PAPP-A across all tissues and both sexes, treating sex, tissue, and treatment as covariates. Red points identify genes differentially expressed at FDR < 0.05. (c) anti-PAPP-A-affected collagen and ECM-related genes across multiple tissues. Cellular component GO terms significantly (FDR < 0.05) enriched in the list of genes differentially expressed by anti-PAPP-A at p < 0.01 in cross-tissue analysis (88 genes). (d) Analysis of differential expression due to anti-PAPP-A across all tissues and both sexes. Red points identify genes in the "collagen-containing extracellular matrix" gene set (GO:0062023). (e) The tissue-specific $\log_2$ fold change for the 29 collagen-containing ECM genes that were affected by anti-PAPP-A across multiple tissues at p < 0.01. (f) *Igfbp5* expression in whole bone marrow. Each point represents the log2 (normalized counts) from RNA-seq data from an individual animal

driven by any single tissue: When we examined the 29 affected genes from the "collagen-containing extracellular matrix" gene set in each tissue individually, we found that most tissues exhibited decreased expression of these genes (Figure 1E). These results demonstrate that adulthood PAPP-A inhibition reduces ECM gene expression across multiple tissues.

2.3 | PAPP-A inhibition reduces osteogenesis via reduced osteoblast activity

The most significant reduction in *Igfbp5* occurred in the bone marrow (Figure 1F), which led us to focus on this tissue to assess functional consequences of PAPP-A inhibition. We treated 18 male and 18 female C57BL/6 mice with anti-PAPP-A or isotype control for 4 months, between 6 and 10 months of age. We then isolated femurs and L5 vertebrae from these animals and analyzed them by micro-computed tomography (μCT). PAPP-A inhibition resulted in a relatively mild, but highly significant, effect on multiple bone parameters in both sexes, both cortical and trabecular, in the femur and the L5 vertebra (Figure 2A, S3A). The overall picture in both sexes is one of reduced bone, leading to reduced thickness and volume with a corresponding increase in relative surface area. For cortical bone, the most consistent effect across both sexes was reduced cortical area (Figure 2B), and for trabecular bone, reduced trabecular thickness (Figure 2C) and associated parameters (e.g., bone surface/volume ratio, which increases as trabeculae become thinner).

In both males and females, anti-PAPP-A resulted in a slight, but significant reduction in weight gain over time (Figure S3B). Bone mass and geometry are affected by body weight, so it was possible that anti-PAPP-A's effect on bone was a result of reduced weight gain. For cortical bone, adjustment for weight effectively eliminated the effect, with no cortical parameters reaching q < 0.05, including cortical area (Figure S3C). In contrast, although adjustment for weight slightly reduced the statistical significance of anti-PAPP-A treatment on trabecular bone, these effects remained highly statistically significant (Figure S3C), suggesting this was a direct effect on bone rather than a by-product of body mass.

Bone is constantly remodeled through a balance between bone resorption and formation. To determine which aspect was affected by PAPP-A inhibition, we performed dynamic histomorphometry on vertebrae and tibiae from these mice, which allows direct quantification of bone formation and resorption rates via injected fluorescent labels that mark bone formed over a known time window (Dempster et al., 2013). The vertebrae of males and females both exhibited decreased bone formation rate (Figure 2D) and trends toward reduced mineralizing surface (MS/BS), osteoblast number (N.Ob/B.Pm), and osteoblast surface (Ob.S/BS) (Figure S3D). As there was no indication of a sex-specific effect, we performed combined-sex statistical analysis, resulting in a statistically significant decrease in bone formation (q = 0.003) and

mineralizing surface (q = 0.046). In the tibia, bone formation rate (BFR/BS), osteoblast numbers (N.Ob/B.Pm), and osteoblast surface (Ob.S/BS) also trended toward a decrease in the anti-PAPP-A animals, with the latter effects being statistically significant in males (Figure S3D). In contrast to the reduced bone formation seen in trabecular bone, there was no effect on dynamic histomorphometry parameters in cortical bone (Figure S3D). Overall, the data show a decrease in trabecular bone formation driven by a decrease in both bone formation rate and osteoblast number, with no effect on bone resorption.

We next asked whether these morphological changes resulted in a weakening of bone, which could have implications for the safety of this potential therapeutic. We subjected femurs to mechanical testing via a 3-point bending to determine the mechanical properties of the bone. Although animals were slightly smaller in the anti-PAPP-A group, after adjustment for bone size, there were no differences between the treatment groups (Figure 2E), suggesting no deficit in the intrinsic properties of the bone material itself.

We also monitored circulating levels of procollagen type 1 propeptides (P1NP), a marker of bone formation, and Tartrate-resistant acid phosphatase (TRACP) 5b, a marker of bone resorption. P1NP declined over the course of the study, consistent with previous reports and indicative of reduced bone formation with age (Weitzmann et al., 2019). There were subtle sex-specific effects, with anti-PAPP-A-treated females showing a slight, but significant, reduction in P1NP over time compared with controls (Figure S3E). For TRACP5b, there was no increased difference between the groups after treatment in either sex, suggesting no anti-PAPP-A effect (Figure S3F). To test another readout of bone resorption, we assayed circulating levels of C telopeptide of type 1 collagen (CTX-1) at the terminal timepoint and saw no effect in either sex (Figure S3G). In summary, PAPP-A inhibition did not have a substantial effect on circulating markers of bone formation or resorption, consistent with anti-PAPP-A having a relatively mild effect on bone.

Bone marrow adiposity is another important component of bone marrow health (Veldhuis-Vlug & Rosen, 2018). To determine whether anti-PAPP-A affects bone marrow adipocytes, we quantified adipocyte volume in the proximal tibia by microscopy. Females exhibited a significant 4–5-fold higher adipose volume and number compared with males. In each sex, we observed a trend toward reduced adipocyte volume vs bone volume (Ad.V/BV) as a result of PAPP-A treatment, which was statistically significant (p = 0.03) when the sexes were combined, with no evidence of a sex-specific effect (Figure 2F). These data demonstrate a mild reduction in bone marrow adiposity in both males and females as a result of anti-PAPP-A treatment.

2.4 | PAPP-A inhibition reduces myelopoiesis

To further characterize the role of PAPP-A-mediated IGF signaling in bone marrow, we examined hematopoiesis. We treated young adult (2–4 months old), male C57BL/6 animals with weekly doses
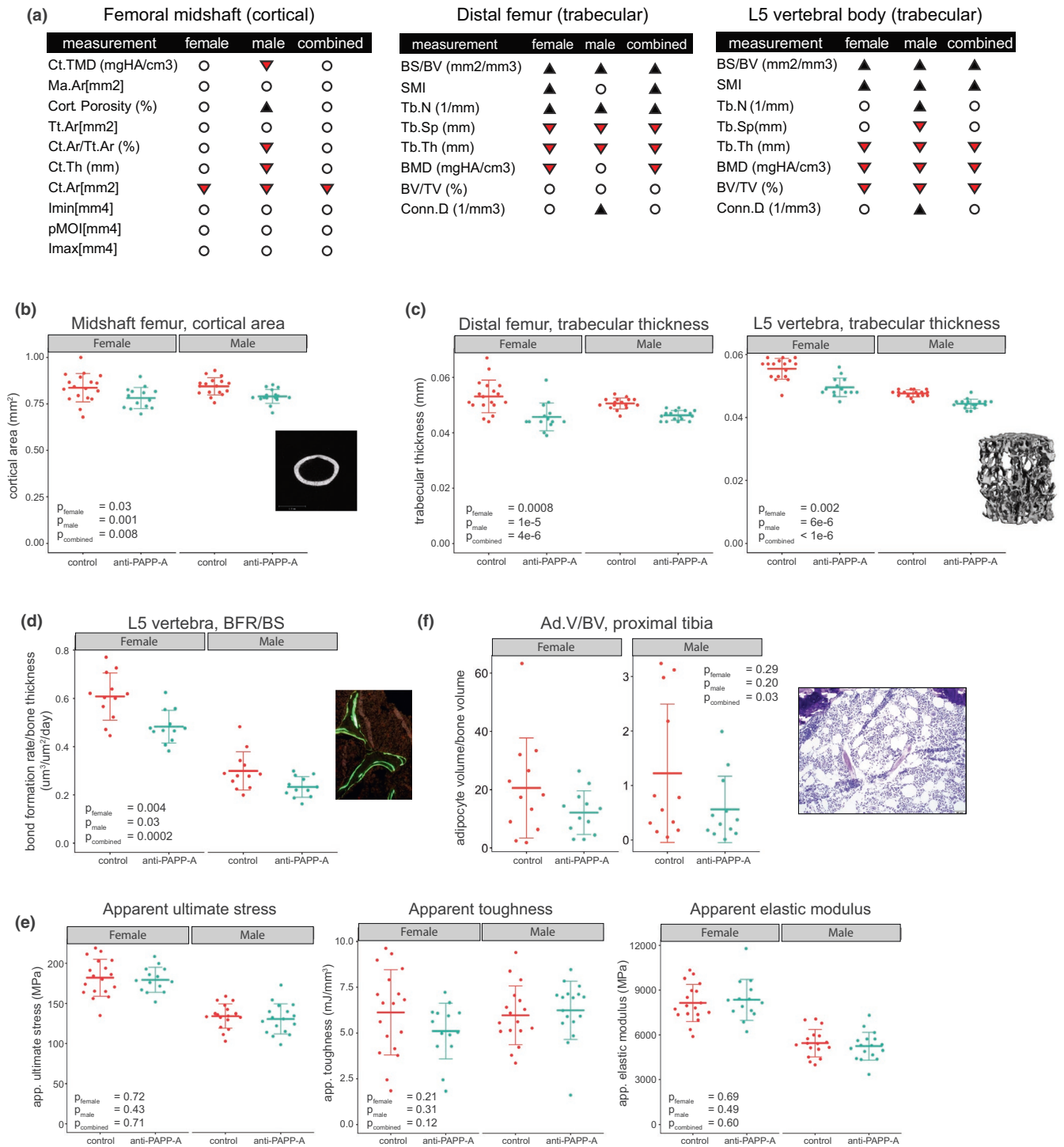
(a)

Femoral midshaft (cortical)

measurement	female	male	combined
Ct.TMD (mgHA/cm3)	o	▼	o
Ma.Ar[mm2]	o	o	o
Cort. Porosity (%)	o	▲	o
Tt.Ar[mm2]	o	o	o
Ct.Ar/Tt.Ar (%)	o	▼	o
Ct.Th (mm)	o	▼	o
Ct.Ar[mm2]	▼	▼	▼
Imin[mm4]	o	o	o
pMOI[mm4]	o	o	o
Imax[mm4]	o	o	o

Distal femur (trabecular)

measurement	female	male	combined
BS/BV (mm2/mm3)	▲	▲	▲
SMI	▲	o	▲
Tb.N (1/mm)	▲	▲	▲
Tb.Sp (mm)	▼	▼	▼
Tb.Th (mm)	▼	▼	▼
BMD (mgHA/cm3)	▼	o	▼
BV/TV (%)	o	o	o
Conn.D (1/mm3)	o	▲	o

L5 vertebral body (trabecular)

measurement	female	male	combined
BS/BV (mm2/mm3)	▲	▲	▲
SMI	▲	▲	▲
Tb.N (1/mm)	o	▲	o
Tb.Sp(mm)	o	▼	o
Tb.Th (mm)	▼	▼	▼
BMD (mgHA/cm3)	▼	▼	▼
BV/TV (%)	▼	▼	▼
Conn.D (1/mm3)	o	▲	o

FIGURE 2 PAPP-A inhibition reduces osteogenesis via reduced osteoblast activity. (a) Summary of effects of anti-PAPP-A on femoral and vertebral bone μCT measurements. Symbols indicate an FDR-corrected significant ($p < 0.05$) reduction (red arrow), increase (black arrow), or no change (o) of bone parameter values for anti-PAPP-A vs. control, separated by sex and with sexes combined. (b) Cortical area of mid-shaft femur, measured by μCT. Image shows a typical cortical scan, white area is quantified. (c) Trabecular thickness in distal femur and L5 vertebra, measured by μCT. Image is a 3D reconstruction of the trabecular bone in a typical L5 vertebral body. (d) Bone formation rate (μm^3) per bone surface (μm^2) per day in L5 vertebra, assessed by dynamic histomorphometry. Image shows a typical histomorphometry image, BFR/BS is related to the distance between labels in double-labeled sections, with a larger distance indicating more bone formation. (e) PAPP-A inhibition did not affect apparent bone material properties. Apparent material properties of femurs derived from three-point bend testing. App. ultimate stress is a geometry-normalized measure of the peak load applied to the bone; app. toughness is a geometry-normalized measure of the work the bone can absorb before fracture; app. elastic modulus is a geometry-normalized measure of the slope of the load-displacement curve prior to inelastic deformation. (f) PAPP-A inhibition reduced bone marrow adipocyte volume/bone volume in the proximal tibia, from the same region used to assess dynamic histomorphometry. Image shows a representative photomicrograph of proximal tibia (Toluidine blue staining; magnification X200); white circles represent adipocyte "ghosts"
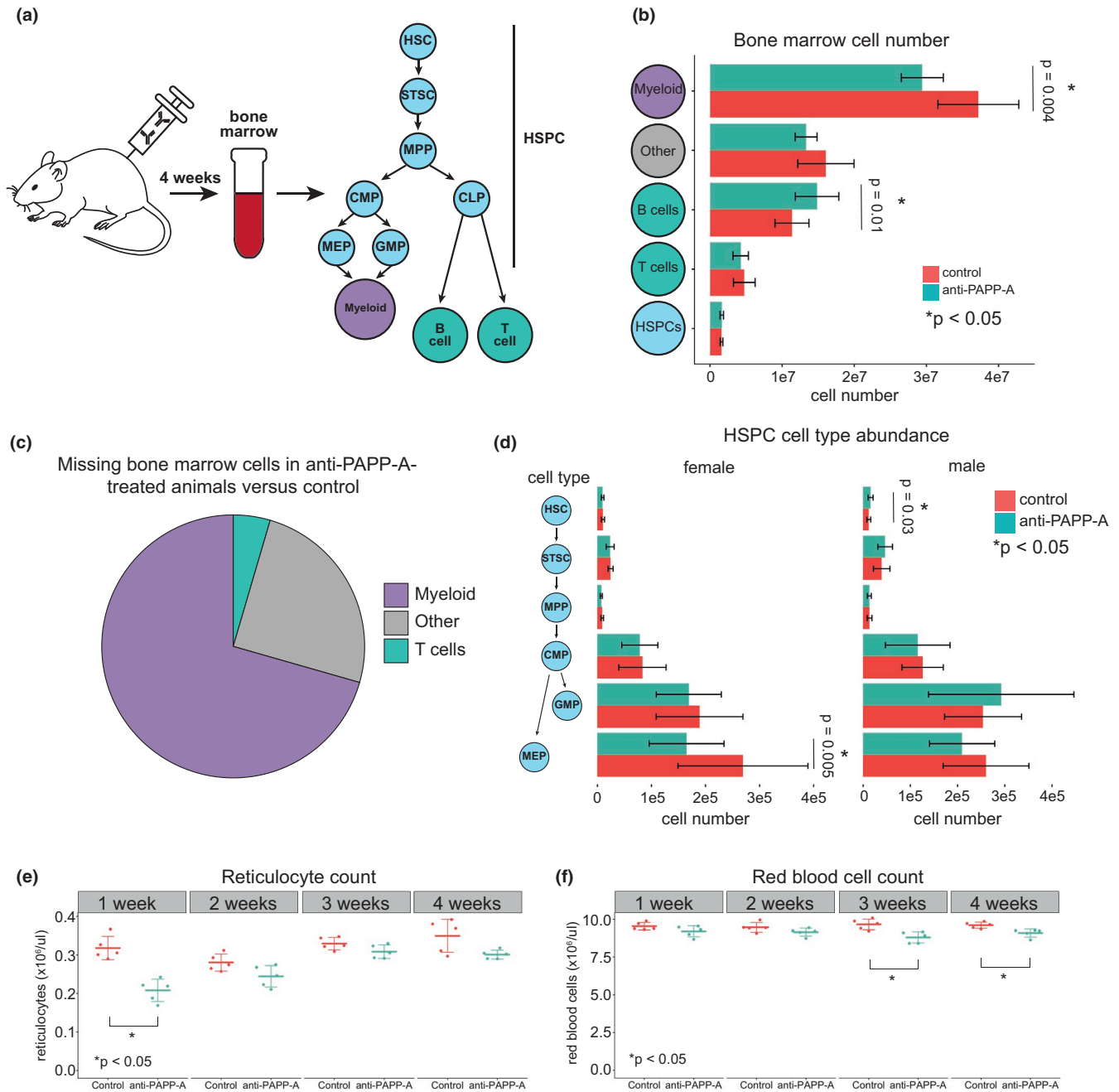
FIGURE 3 PAPP-A inhibition reduces myelopoiesis. (a) Experimental design, indicating isolated cell types and their hierarchical relationship to one another. HSC = hematopoietic stem cell, STSC = short-term stem cell, MPP = multipotent progenitor cell, CMP = common myeloid progenitor, CLP = common lymphoid progenitor, MEP = megakaryocyte/erythrocyte progenitor, GMP = granulocyte-macrophage progenitor. (b) PAPP-A inhibition reduced myeloid cell number in bone marrow. Abundance of each cell type in bone marrow after 4 weeks of treatment with anti-PAPP-A (males only, *n* = 10/group). (c) Myeloid cells accounted for the majority of cells lost from the bone marrow after 4 weeks of PAPP-A inhibition. Same data as 3B, showing contribution of each cell category to missing cells in anti-PAPP-A group (males only, *n* = 10/group). (b) PAPP-A inhibition had minimal effect on HSPC abundance. Abundance of each cell type in bone marrow after 4 weeks of treatment with anti-PAPP-A (*n* = 15/sex/group). (c) PAPP-A inhibition transiently reduced reticulocyte number. Reticulocyte count in circulation after 1–4 weeks of treatment with anti-PAPP-A (males, only, *n* = 5/group). (d) PAPP-A inhibition reduced red blood cell count. Red blood cell count in circulation after 1–4 weeks of treatment with anti-PAPP-A (males only, *n* = 5/group)

of anti-PAPP-A or isotype control and isolated bone marrow from the leg bones 4 weeks later (Figure 3A), choosing that treatment time because we reasoned that changes in cell proportions would become evident more quickly than changes in bone. At 4 weeks,

anti-PAPP-A-treated mice exhibited a trend toward reduced bone marrow cellularity (Figure S4A), which was largely driven by a decrease in committed myeloid cells (CD11b+) (Figure 3B, 3C) as compared to other major cell categories: B cells, T cells, hematopoietic

stem and progenitor cells (HSPCs), and other cell types that we did not specifically stain for ("Other"). To test the robustness of this finding, we repeated the experiment with more animals and both sexes: n = 15 males and 15 females/group. Bone marrow cellularity was reduced, significantly in females and non-significantly in males, though the average effect size was similar in both (Figure S4B), and this was again primarily driven by a reduction in myeloid cells (Figure S4C). Further suggesting this was primarily a myeloid effect, there were no significant changes in the total or fractionated cellularities of the spleen, a primarily lymphoid organ (Figure S4D, S4E).

To understand where in the myelopoiesis pathway this cell loss began, we examined HSPCs in more detail. In both the original (males only) and validation studies (males and females), there was no decrease in hematopoietic stem cells (HSCs), short-term stem cells (STSCs), or multipotent progenitors (MPPs), which can differentiate into myeloid and lymphoid lineages (Figure 3D, S4F). There was, however, a significant reduction in megakaryocyte/erythrocyte progenitors (MEPs) in females and a trend in that direction in males (Figure 3D), suggesting that the reduction in myelopoiesis may begin once myeloid commitment has occurred.
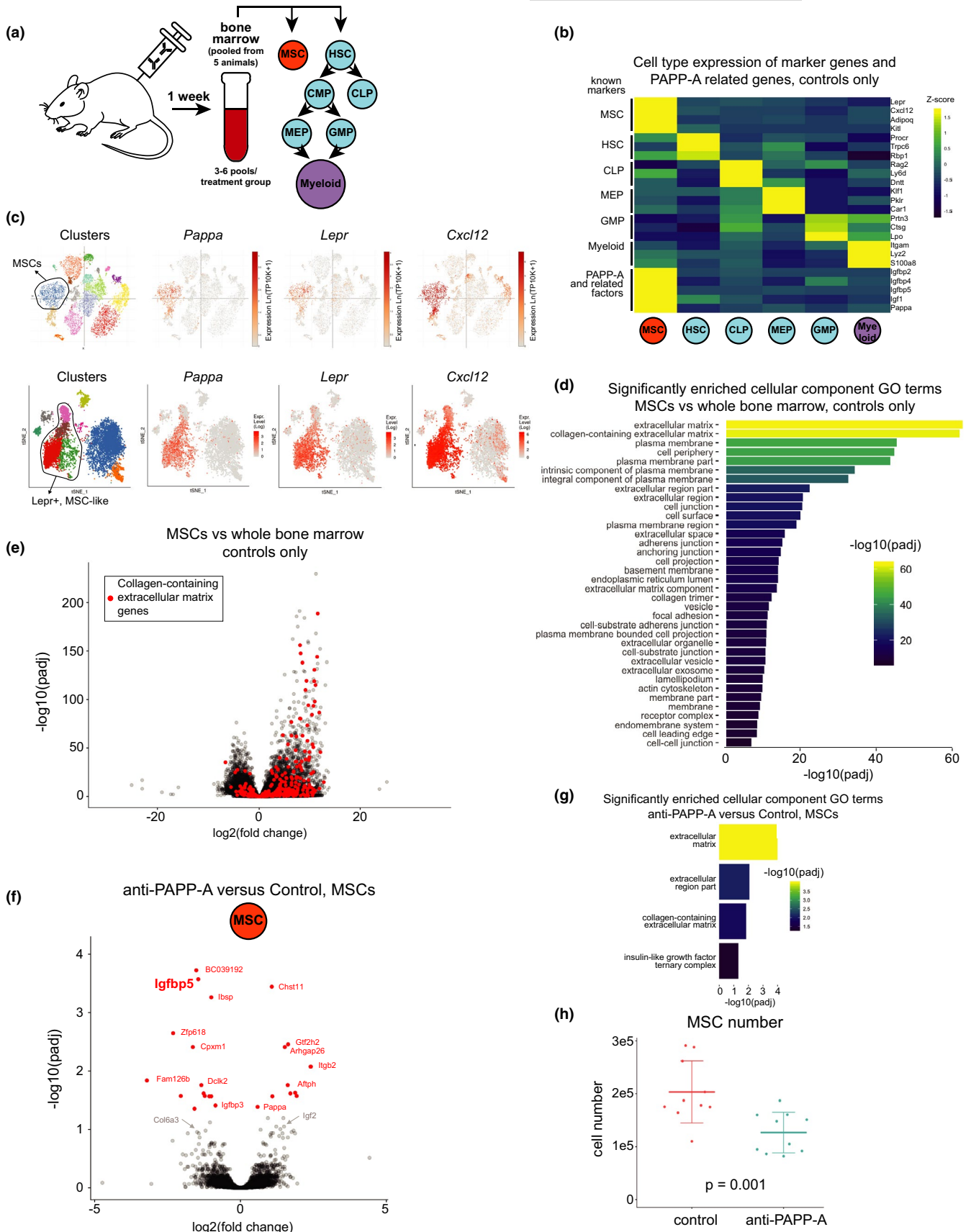
To determine whether these bone marrow effects resulted in changes to circulating blood cells, and how quickly, we treated young adult (2–4 months old), male C57BL/6 animals with weekly doses of anti-PAPP-A or isotype control and measured blood cell populations every week for four weeks. After one week, there was a striking reduction in reticulocyte counts (Figure 3E), which later recovered and stabilized as a small reduction in red blood cells (Figure 3F). Hemoglobin and hematocrit were also reduced at some timepoints (Figure S4G). In contrast, there was no effect on platelet or white blood cell counts (Figure S4H). We found that bone marrow cellularity changes were also detectable at this earlier timepoint—7 days after a single dose of anti-PAPP-A, bone marrow cellularity was significantly reduced (Figure S4I). These data demonstrate that the lineage-specific effects on hematopoiesis that arise in the bone marrow due to anti-PAPP-A give rise to differences in circulating blood cell populations.

2.5 | MSCs are the primary source of PAPP-A in bone marrow and depend on PAPP-A for persistence

To better understand the bone marrow phenotypes caused by anti-PAPP-A treatment, we analyzed different cell populations within the bone marrow. Bone marrow consists of both hematopoietic cells, produced by HSCs, and the stroma, which largely consists of mesenchymal and endothelial cell types (Kfoury & Scadden, 2015; Orkin & Zon, 2008), including MSCs. MSCs are rare populations of non-hematopoietic, multipotent cells that are found across tissues in the stroma or perivascular niches and serve as progenitors of connective tissues (osteo-, adipo-, and chondrocyte lineages), as well as organizers of tissue niches (Crisan et al., 2008; Kfoury & Scadden, 2015; Meirelles et al., 2006). To characterize which bone marrow cells types were involved in IGF signaling and acutely responsive to PAPP-A inhibition, we treated 8-week-old male C57BL/6 animals with a single dose of anti-PAPP-A or isotype control, then isolated bone marrow one week later and fractionated HSPCs and MSCs (Figure 4A). We chose this short timeframe because we reasoned that gene expression changes would become evident more rapidly than changes in cell proportions. Because most of these cell types are very rare (e.g. ~0.3% for MSCs, ≤0.05% for HSCs), we pooled the bone marrow from 5 mice per replicate, with 3–6 replicates per treatment group. We then assessed the transcriptome of each of these cell types via RNA-seq.

We confirmed that this sorting paradigm effectively separated cell types by measuring known markers, including *Lepr*, *Cxcl12*, *Adipoq*, and *Kitl* as markers of MSCs (Baryawno et al., 2019; Giladi et al., 2018; Nestorowa et al., 2016; Tikhonova et al., 2019) (Figure 4B). Further, isolated MSCs were able to differentiate into osteoblasts in culture, confirming their progenitor cell identity (Figure S5A). Interestingly, when we examined the cell type-specific expression of *Pappa*, its substrates (*Igfbp2*, *Igfbp4*, *Igfbp5*), and its downstream effector, *Igf1*, we saw marked enrichment of all these mRNAs in MSCs as compared to HSPCs or myeloid cells (Figure 4B). Recent single cell RNA-sequencing (scRNA-seq) studies of murine bone marrow stroma have

FIGURE 4 MSCs are the primary source of PAPP-A in bone marrow and depend on PAPP-A for persistence. (a) Experimental design, indicating isolated cell types and their hierarchical relationship to one another. MSC = mesenchymal stromal cell, HSC = hematopoietic stem cell, CMP = common myeloid progenitor, CLP = common lymphoid progenitor, MEP = megakaryocyte/erythrocyte progenitor, GMP = granulocyte-macrophage progenitor. (b) Cell type-specific expression of known marker genes and PAPP-A-related genes. Control animals only. Colors represent z-scores of log2 normalized counts. (c) *Pappa* is expressed in MSCs and Lepr+, MSC-like cells. t-SNE plots depicting scRNA-seq data from mouse bone marrow stroma from Baryawno et al., *Cell*, 2019 (top) and Tikhonova et al., *Nature*, 2019 (bottom). *Lepr* and *Cxcl12* are MSC markers. Plots are colored by expression of indicated genes or by post hoc clustering. Figures adapted, with permission, from: https://singlecell.broadinstitute.org/single_cell/study/SCP361/ and http://aifantislab.com/niche/. (d) MSCs expressed high levels of collagen and ECM-related genes. Cellular component GO terms enriched (FDR <1e-7 for brevity) in the list of genes differentially expressed (FDR <0.01, |log2FC| >3) by MSCs versus whole bone marrow (2557 genes). Control animals only. (e) Analysis of differential expression of MSCs versus whole bone marrow. Control animals only. Red points identify genes in the "collagen-containing extracellular matrix" gene set (GO:0062023). (f) Differential expression due to anti-PAPP-A in MSCs. Red points identify genes differentially expressed at FDR <0.05. (g) anti-PAPP-A-affected collagen/ECM-related genes and IGF signaling in MSCs. Cellular component GO terms enriched (FDR <0.05) in the list of genes differentially expressed by anti-PAPP-A at *p* < 0.005 in MSCs (105 genes). (h) anti-PAPP-A reduced MSC cell number in bone marrow after 4 weeks of treatment (males only, n = 10/group)

(a)

(b) Cell type expression of marker genes and PAPP-A related genes, controls only

(c) Clusters | Pappa | Lepr | Cxcl12

(d) Significantly enriched cellular component GO terms MSCs vs whole bone marrow, controls only

(e) MSCs vs whole bone marrow controls only

(f) anti-PAPP-A versus Control, MSCs

(g) Significantly enriched cellular component GO terms anti-PAPP-A versus Control, MSCs

(h) MSC number

characterized non-hematopoietic cell populations in detail, and when we examined those datasets we found that, consistent with our results, *Pappa* was highly enriched in cells positive for the MSC markers *Lepr* and *Cxcl12* (Baryawno et al., 2019; Tikhonova et al., 2019) (Figure 4C). Thus, MSCs represent the primary source of PAPP-A in the bone marrow, as well as being major producers of other IGF signaling components.

Using control-treated animals, we examined the general pattern of gene expression in each cell type relative to whole bone marrow, focusing on MSCs because of their high PAPP-A expression. Thousands of genes were significantly differentially expressed in the sorted MSCs relative to whole bone marrow, and when we subjected the top genes (FDR <0.01, |log2FC| >3, 2557 genes) to GO term analysis, we identified a clear enrichment in GO terms related to ECM, of which "collagen-containing extracellular matrix" was second most significant (adj p = 8.8e-47) (Figure 4D). Visual inspection of the 334 genes in this gene set on the MSC volcano plot indicated a general increase in gene expression across the entire set (Figure 4E). We conclude that MSCs are both the primary source of PAPP-A in bone marrow and producers of the ECM genes downregulated by anti-PAPP-A. Of note, recent scRNA-seq analyses have shown that MSC-derived cells, namely fibroblasts and osteolineage cells, are even greater producers of ECM in the bone marrow than MSCs themselves (Baryawno et al., 2019; Tikhonova et al., 2019). The production of PAPP-A by MSCs and the production of ECM by MSCs and MSC-derived cells suggested that MSCs may be the primary mediators of the effect of anti-PAPP-A on ECM gene expression.

To test this hypothesis, we examined the response of each cell type to PAPP-A inhibition. HSPCs showed a few differentially expressed genes, none of which were related to IGF signaling or ECM production (Figure S5B, Table S1). Analyzing HSPC cell types individually (HSC, CLP, MEP, GMP) also yielded few significantly changed genes (Figure S5C, Table S2). A handful of genes were also differentially expressed in myeloid cells, again, without any enrichment for IGF signaling or ECM production (Figure S5D, Table S2). In all cases, GO analysis yielded only general terms (e.g., nucleic acid binding) without strong enrichment. Notably, *Igfbp5* was not decreased in any of the HSPC or myeloid cell types (Figure S5E), suggesting unaltered IGF signaling in these cells. In contrast, MSCs showed a larger number of differentially expressed genes, the second most significant of which was *Igfbp5* (Figure 4F). Interestingly, *Pappa* itself was slightly but significantly upregulated, and *Igf2* showed a trend toward upregulation, suggesting a partial compensatory response. When we submitted the top 105 genes affected by PAPP-A inhibition (p < 0.005) to GO term analysis, we saw significant enrichment for the same ECM GO terms that we identified previously (Figure 4G), whereas no such enrichment was found for HPSC or myeloid cell types, irrespective of statistical cutoff. These data, particularly the notable reduction in *Igfbp5* after a single dose of anti-PAPP-A, support the hypothesis that MSCs are the proximal responders to anti-PAPP-A in the bone marrow.

Given the strong reduction in IGF signaling (measured by reduced *Igfbp5*), we hypothesized that anti-PAPP-A might alter MSC cell number. To address this, we treated 8-week-old male C57BL/6 animals with anti-PAPP-A or isotype control for 4 weeks and measured bone marrow MSC numbers. We observed a striking ~40% reduction in MSC number in both males and females, across two independent experiments (Figure 4H, S6A). We observed a similar decrease in MSC number 7 days after a single dose of anti-PAPP-A, highlighting the acute nature of this response (Figure S6B). To expand these findings, we also examined MSCs in 3- to 6-month-old PAPP-A KO mice. We report frequency rather than absolute number, as PAPP-A KO mice are ~60% the size of WT mice. Similar to anti-PAPP-A-treated animals, PAPP-A KO mice exhibited a reduction in MSC content (combined p = 0.035; Figure S6C). Taken together, these results support a model in which anti-PAPP-A reduces IGF signaling in MSCs, which reduces their survival and/or proliferative ability and leads to a reduction in cell number over time.

To determine whether these effects would be expected to counteract age-related changes, we measured bone marrow cellularity and MSC number in young (5 months) and old (20 months) wild-type, untreated mice. Both bone marrow cellularity and MSC number were significantly increased with age (Figure S6D,E). Therefore, the effect of anti-PAPP-A on bone marrow cellularity and MSC number is opposite normal aging trends in this tissue.

2.6 | PAPP-A is expressed by MSC-like cells in multiple tissues

Bone marrow-derived MSCs represent the most-studied multipotent stromal cell subtype, but virtually all adult tissues contain an MSC-like population (Crisan et al., 2008; Meirelles et al., 2006). We hypothesized that the system-wide decrease in ECM genes upon PAPP-A inhibition (from Figure 1) arises through modulation of MSC-like cells in multiple tissues, and as a first step in testing this hypothesis, we examined whether PAPP-A was highly expressed in the MSCs of other tissues, using available scRNA-seq datasets.

The Tabula Muris is one of the broadest scRNA-seq datasets currently available, containing data for twenty mouse tissues (The Tabula Muris Consortium, 2018). In this dataset, stromal cell populations from multiple tissues showed enrichment for *Pappa* gene expression, including stellate cells from the pancreas, which are thought to be a MSC-like population (Zhou et al., 2019), fibroblasts from the heart, and MSCs from trachea, adipose, lung, muscle, and mammary gland (Figure 5A). Of note, the Tabula Muris bone marrow isolation procedure enriched for hematopoietic populations, and therefore, bone marrow MSCs are not part of this dataset. A similar multi-tissue scRNA-seq dataset was recently published using a different methodology than the Tabula Muris, and this dataset also showed strong enrichment of *Pappa* gene expression in stromal cell populations from multiple tissues,
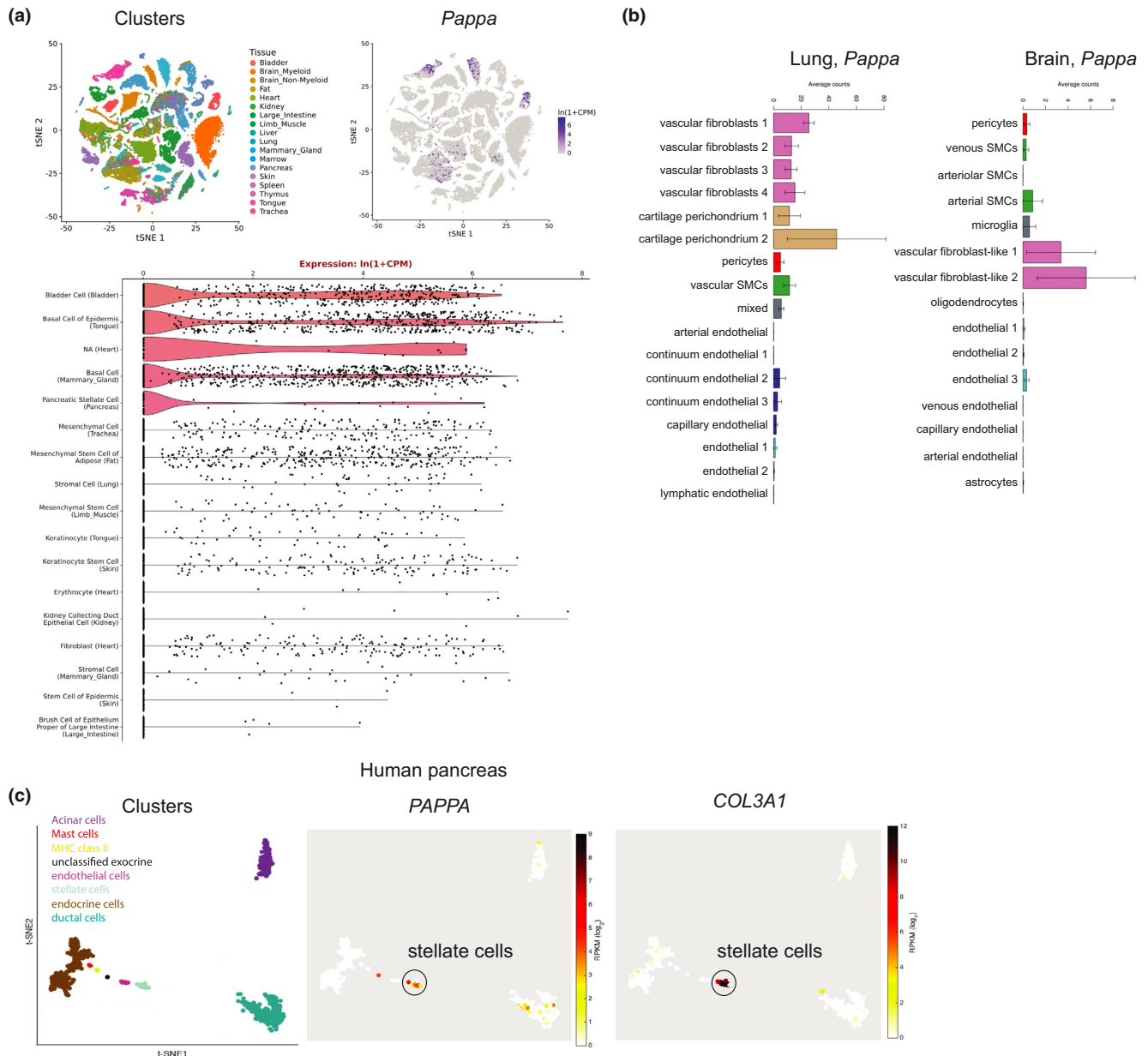
FIGURE 5 PAPP-A is expressed by MSC-like cells in multiple tissues (a) scRNA-seq data from mouse tissues, Tabula Muris. *Pappa* is expressed in mesenchymal stem/stromal populations from multiple tissues. Figure adapted from https://tabula-muris.ds.czbiohub.org/. (b) scRNA-seq data from mouse brain, Vanlandewijck et al., 2018. *Pappa* is expressed in vascular fibroblast-like cells. Figure adapted from http://betsholtzlab.org/VascularSingleCells/database.html. (c) scRNA-seq data from human pancreas, Segerstolpe et al., 2016. *PAPPA* is expressed in stellate cells. Figure adapted from http://sandberg.cmb.ki.se/pancreas/

including the bone marrow stroma (CXCL12-high cells) and lung stroma (mesenchymal alveolar niche cells and stromal cells) (Han et al., 2018).

We explored several other scRNA-seq datasets, including one of vascular-associated cells in the mouse lung and brain (He et al., 2018; Vanlandewijck et al., 2018). Consistent with perivascular MSC expression, this dataset showed *Pappa* gene expression enriched in "perivascular fibroblast-like cells" in both tissues (Figure 5B). These fibroblast-like cells were also enriched for collagen and ECM expression, consistent with an MSC-like phenotype.

We also examined a scRNA-seq dataset from human pancreas (Segerstolpe et al., 2016). Similar to the mouse pancreas from the Tabula Muris, this dataset showed an enrichment of *PAPPA* gene expression in the MSC-like pancreatic stellate cells, which also expressed high levels of collagen and ECM genes (Figure 5C). These data demonstrate that multiple tissues in humans and mice harbor cells expressing relatively high levels of PAPP-A and that these cells exhibit gene expression signatures, annotations, lineage, and anatomical location (perivascular) that are reminiscent of bone marrow MSCs.

3 | DISCUSSION

Reduced IGF signaling delays aging and age-related pathologies in multiple species and contexts, making PAPP-A inhibition a promising therapeutic strategy. In spite of this, PAPP-A remains an understudied factor, with unresolved questions about where and when it is expressed, as well as its effect on different tissues and cell populations. Thus, the mechanism by which its inhibition extends longevity remains opaque.

To address this, we developed a specific and potent neutralizing antibody against PAPP-A and used it to study the tissue, cellular, and transcriptomic consequences of adult PAPP-A inhibition. Our experiments utilized adult, wild-type animals in order to model the effects of dosing an aging, but otherwise healthy, adult human population. Starting with multi-tissue transcriptomics, we found that PAPP-A plays a clear functional role during adulthood across multiple tissues. System-wide, PAPP-A inhibition decreased IGF signaling as measured by *Igfbp5* mRNA level (Duan et al., 1996; Fleming et al., 2005; Harrington et al., 2007; Kuemmerle, 2000; Resch et al., 2006; Swindell et al., 2010; Ye & D'Ercole, 1998). Reduced *Igfbp5* was, in fact, the most significant response across the entire transcriptome, highlighting the precise targeting of anti-PAPP-A. That PAPP-A inhibition can modulate IGF signaling across a wide breadth of tissues and organs without triggering somatotropic compensation in the form of increased circulating IGF-1 or GH is remarkable and points to local modulation of IGF as an underappreciated dimension of IGF signaling.

Not only did PAPP-A inhibition widely reduce IGF signaling, but it also had a previously unknown effect on system-wide ECM gene expression: anti-PAPP-A caused a coordinated downregulation of ECM genes across the nine tissues we examined. To deeply understand the effects of PAPP-A inhibition and to uncover the mechanism behind the reduction in ECM gene expression, we focused on one tissue, the bone marrow, which exhibited the strongest reduction in IGF signaling. We characterized the effect of PAPP-A inhibition on major functions of this organ: bone homeostasis, marrow adiposity, and hematopoiesis. Surprisingly, we found that all were reduced. This shows that PAPP-A regulates adult bone marrow function; however, these diverse effects were challenging to fit into a coherent model. To address this, we profiled PAPP-A expression in multiple bone marrow cell types via FACS sorting and examined publicly available scRNA-seq datasets. Both approaches identified MSCs as the primary producers of *Pappa*. MSCs are also reliant on PAPP-A-mediated IGF signaling, as a single dose of anti-PAPP-A reduced IGF signaling in MSCs and dramatically reduced their number. No other cell type we examined exhibited a similar response, suggesting MSCs are the proximal responders to PAPP-A inhibition.

These rare but important cells link the phenotypes caused by PAPP-A inhibition: MSCs (1) have a transcriptomic profile strongly enriched for ECM production and are the progenitors of fibroblasts

and other ECM-depositing cells, (2) are the originating source of adult bone (Zhou et al., 2014), (3) regulate marrow adiposity (Veldhuis-Vlug & Rosen, 2018), and (4) are essential components of the hematopoietic niche (Ding et al., 2012; Kfoury & Scadden, 2015; Zhou et al., 2014). Our data suggest that PAPP-A inhibition mediates its broad effects on bone marrow via modulation of MSC number and activity (Figure 6, blue box). Further, we found that MSC-like cells in other human and murine tissues are also major producers of PAPP-A, providing a plausible mechanism for the observed multi-tissue effects on gene expression. We believe this model represents the most parsimonious explanation of our observations, but it is also possible that the effects on ECM production, bone, and myelopoiesis are independent of the effects on MSCs; future work may address this by genetically inhibiting PAPP-A-mediated IGF signaling specifically in MSCs and assessing tissue-level consequences.

Here, we identify MSCs as a novel source of PAPP-A, but previous reports have shown that PAPP-A is also expressed by smooth muscle cells (SMCs) in vitro and in vivo during response to vascular injury, such as angioplasty or plaque formation (Bayes-Genis et al., 2001; Conover et al., 2006; Hjortebjerg, 2018; Resch et al., 2006). At first glance, this seems unrelated to MSC-produced PAPP-A. However, in response to vascular injury, SMCs adopt a "synthetic" phenotype, that is, an ECM-producing, mesenchymal-like phenotype, and this state is associated with an upregulation of multiple IGF signaling components (Dobnikar et al., 2018; Wirka et al., 2019). Standard culture serum induces a synthetic SMC phenotype (Wenzel & Balzar, 2006), which may be why SMCs in vitro express high levels of PAPP-A. Conversely, most SMCs in healthy tissues produce little, if any, PAPP-A (Suryawanshi et al., 2018; The Tabula Muris Consortium, 2018). Therefore, we speculate that the expression of PAPP-A from SMCs during vascular injury is caused by a shift to a mesenchymal-like state that engages regulatory mechanisms similar to those in MSCs.

The production of PAPP-A by MSCs and their dependence on PAPP-A-mediated IGF signaling could explain multiple phenotypes of PAPP-A mutant mice. MSCs localize to the abluminal side of the vasculature, giving them a broad but sparse tissue distribution (Crisan et al., 2008; Kramann et al., 2015). This patterning may explain the relatively low, but pervasive, expression of PAPP-A across tissues (Harstad & Conover, 2014). PAPP-A KO mice are resistant to fat accumulation on a high-fat diet (Conover et al., 2013; Tanner et al., 2008). Since adipocytes derive from tissue-resident MSCs, and preadipocytes exhibit many similarities to bone marrow MSCs (Cawthorn et al., 2012), the reduced adiposity of PAPP-A KO mice may results from reduced number and/or size of MSC-derived adipocytes. PAPP-A KO mice are also resistant to atherosclerotic plaque progression and neointima formation (Conover et al., 2016; Harrington et al., 2007; Resch et al., 2006). Plaque progression is enhanced by inflammatory activation of a pro-ECM phenotype in perivascular MSC-like cells and the expansion of "synthetic," that is, mesenchymal-like, SMCs (Mingjun and Delphine, 2019). Thus, it

FIGURE 6 Model of PAPP-A effects during normal tissue homeostasis and aging. This manuscript demonstrates that PAPP-A is expressed by MSCs and potentiates IGF signaling in those cells, increasing their activity and/or proliferation and promoting normal tissue function such as ECM production, myeloid cell production, and bone marrow osteogenesis and adipogenesis. However, with age, PAPP-A-mediated IGF stimulation in MSCs may become maladaptive, leading to aberrant collagen/ECM deposition that drives fibrosis-related pathology, and/or MSC functional exhaustion that drives tissue dysfunction. We hypothesize that restraining MSC activity and thereby delaying these fates is the mechanism by which PAPP-A inhibition extends healthspan and lifespan. Figure created with biorender.com
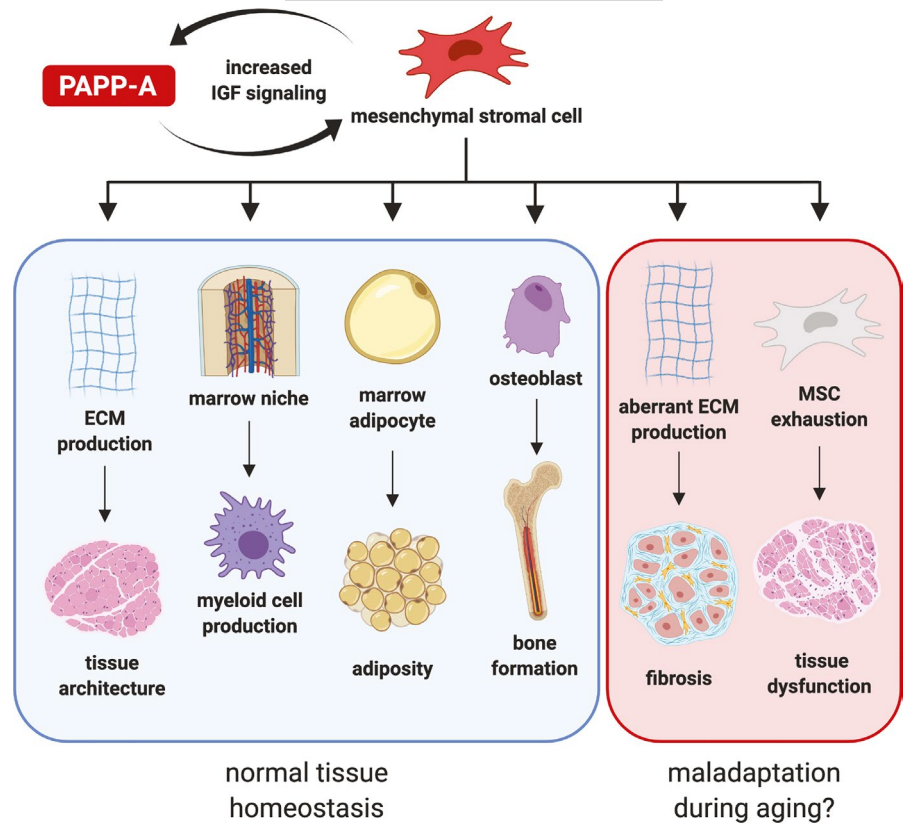
is plausible that PAPP-A inhibition delays atherosclerosis by reducing the activation or expansion of these cell types. Lastly, PAPP-A KO mice exhibit delayed fracture repair (Miller et al., 2007). MSCs play a role in normal wound-healing responses, including fracture repair (Maxson et al., 2012; Shi et al., 2017; Zhou et al., 2014), so this phenotype may be explained by reduced MSC number in PAPP-A KO mice, and PAPP-A inhibition may alter the dynamics of wound-healing responses more broadly. We have not investigated the effect of PAPP-A inhibition in wound healing, but PAPP-A is expressed in healing human skin (Chen et al., 2003), so we view this as a plausible hypothesis.

The association of PAPP-A expression with human pathologies may also be linked to its role in MSC biology. Aberrant MSC activation has been implicated in fibrosis in multiple organs, including kidney, heart, lung, liver, skin, and bone marrow (El Agha et al., 2017). The expansion of MSCs may explain the increase in *PAPPA* and *IGFBP* gene expression recently observed in human fibrosis (Freese et al., 2016; Schafer et al., 2017). Circulating levels of PAPP-A are elevated in patients with acute coronary syndrome and are predictive of poor outcome (Loncar and Haehling, 2014). The source of circulating PAPP-A is unknown, but could be inflammation-activated perivascular MSCs, as PAPP-A has been shown to increase in response to cytokine stimulation in multiple mesenchymal cell types (Conover et al., 2004, 2006; Resch et al., 2004). Further, high *PAPPA* gene expression is associated with

poor outcome in breast cancer patients; transcriptomic analysis shows that patients with high *PAPPA* expression also have heightened levels of ECM genes (Slocum et al., 2019).

Lastly, and perhaps most importantly, PAPP-A inhibition extends longevity, and this effect may also be mediated by MSCs (Figure 6, red box). In the context of age-related pathologies such as fibrosis, MSCs are hyperactivated, becoming myofibroblast-like and aberrantly expanding while depositing collagen and ECM, compromising organ structure and function (El Agha et al., 2017). However, normal aging is also associated with reduced collagen and ECM gene expression across multiple tissues (de Magalhaes et al., 2009; Schaum et al., 2020; Sprenger et al., 2010), perhaps indicating reduced MSC activity due to their functional exhaustion despite increased MSC number. More work is needed to understand how PAPP-A inhibition affects these divergent aging patterns, but it may be that, by restraining MSC activity, PAPP-A inhibition both prevents aberrant MSC activation and delays MSC exhaustion, thereby preserving MSC functional lifespan. Thus, restraining MSC activity may be the mechanism by which PAPP-A inhibition extends longevity and delays aging in multiple tissues.

In summary, our results expand the understanding of the importance of local IGF signaling in multiple adult tissues and identify this pathway as an essential component of bone marrow and MSC homeostasis in vivo. This is a key finding, as knowing the cell

types that rely on IGF signaling is an essential step in developing IGF-modulating therapies. This new knowledge, coupled with the established phenotypes of PAPP-A KO mice, hints at multiple therapeutic avenues for PAPP-A inhibitors. PAPP-A neither eliminates IGF signaling nor completely ablates MSCs; rather, it acts as a dimmer switch such that normal activity remains relatively intact, but MSC dysregulation in the context of aging may be prevented. Reduced IGF signaling has been a compelling longevity target for decades; PAPP-A inhibition seems to provide a safe and effective path toward that goal, with this study adding to our understanding of the relevant cellular mechanisms.

4 | EXPERIMENTAL PROCEDURES

4.1 | Study design

Previous studies have implicated PAPP-A inhibition in the extension of lifespan and healthspan, but the mechanism behind this effect is unknown, as is the effect of shorter-term PAPP-A inhibition. The main goal of our study was to evaluate the tissue, cellular, and transcriptomic consequences of a PAPP-A neutralizing antibody in vivo. Sample sizes were calculated by power analysis from pilot studies and/or by our experience measuring the pre-specified endpoints. Animal enrollment age was determined by availability and in all cases was restricted to 2–6 months of age, that is, young adulthood. Mice were randomized to treatment group by body weight. For most experiments, investigators were blinded to which intervention each animal received, and measurements (e.g., bone parameters, ELISAs, FACS-based cell counts) were blinded until statistical analysis. Endpoints were chosen on the basis of our expertise and were prospectively selected. In cases where multiple endpoints were assessed, FDR correction has been applied. No outliers were excluded from analysis.

4.2 | In vitro PAPP-A enzymatic cleavage of IGF-binding proteins

Human and murine PAPP-A proteins with C-terminal C-myc and Flag tags were expressed by stably transduced HEK293 cell line and purified by heparin column chromatography. Human and murine IGFBP-2, IGFBP-4, and IGFBP-5 proteins were produced recombinantly by transient expression in HEK293 cells with either N-terminal (for human proteins) or C-terminal (for murine proteins) 6His tag and purified by Ni-Sepharose column chromatography. For enzymatic cleavage reactions, IGFBP-2 and IGFBP-4 proteins were pre-incubated with IGF1 of appropriate species (R&D Systems, 291-G1-200 for human and 791-MG-050 for mouse) for 30 min at 37°C. IGFBP-2/IGF1, IGFBP-4/IGF1, or IGFBP-5 proteins were then mixed with various concentrations of PAPP-A and incubated for 2–4 hours at 37°C. Final concentration in cleavage

reactions was 90 nM for IGFBPs and 850 nM for IGF1. Proteins were then resolved by capillary electrophoresis on Wes instrument (ProteinSimple) using capillary cartridge kit (ProteinSimple, cat. # SM-W002-1), probed with THE HisTag antibody (GeneScript, cat. # A00186) and visualized with anti-mouse detection module (ProteinSimple, cat. # DM-002). To evaluate neutralizing potency of anti-PAPP-A antibody, PAPP-A protein was pre-incubated with various concentrations of anti-PAPP-A antibody prior to adding to IGF1/IGFBP-4 mix. PAPP-A concentration in these assays was fixed to 0.4 nM for IGFBP-4, 3.5 nM for IGFBP-2, and 0.08 nM for IGFBP-5 cleavage.

4.3 | Cellular pAKT assay

IGFBP-4 protein was mixed with IGF1 and incubated for 30 min at 37°C. PAPP-A protein was added to IGFBP-4/IGF1 mix and incubated for 4–5 hours at 37°C. Final concentrations in the reaction were 90 nM for IGFBP-4, 15 nM for IGF1, and 0.6 nM for PAPP-A. HEK293 cells were plated in EMEM media without serum and allowed to adhere overnight. IGF1/IGFBP-4/PAPP-A mix was added to cells at 1:30 final dilution and incubated for 20 min at 37°C. Cells were lysed in MSD Tris Lysis buffer and analyzed by Phospho(Ser473)/Total Akt Whole Cell Lysate kit (MSD, K15100D) according to manufacturer's protocol. To evaluate neutralizing potency of anti-PAPP-A antibody, PAPP-A protein was pre-incubated with various concentrations of anti-PAPP-A antibody prior to adding to IGF1/IGFBP-4 mix.

4.4 | Antibody production and validation

Anti-PAPP-A antibody with mouse IgG1 isotype was produced by transient transfection of HEK293 cells and purified by protein-A chromatography. The protein was estimated to be 98.9% monomer by SEC chromatography and had endotoxin of less than 0.27 EU/mg. Binding kinetics of anti-PAPP-A antibody to both human and mouse PAPP-A was evaluated by SPR with antibody capture on chip CM5 and PAPP-A concentrations ranging from 0.78 to 100 nM. Pharmacokinetic profile of anti-PAPP-A antibody was evaluated by single-dose IV injection of 5 mg/kg in C57BL/6 male mice. Antibody blood concentration was measured by direct ELISA with PAPP-A protein.

4.5 | Mice

Male and female C57BL/6 wild-type (WT) mice were purchased from The Jackson Laboratory (strain #000664) at 2–6 months of age. Once at Calico or AbbVie, mice were housed 3–5 mice to a cage and underwent a minimum 3-day acclimation period prior to placement on study. Mice were maintained on a 12:12-hour light:dark

cycle at 22°C with environmental enrichment (e.g., nesting material and/or huts) with access to water and food ad libitum. All studies were performed in adherence to the NIH Guide for the Care and Use of Laboratory Animals.

PAPP-A knock-in reporter mice were generated by The Jackson Laboratory using standard CRISPR/Cas9 methods. Briefly, a P2A-HA-Luciferase-EGFP-bGHpA cassette was inserted in-frame into exon 2 of *Pappa* (NC_000070.6). These mice report PAPP-A expression while disrupting expression of endogenous *Pappa*, and thus, homozygous reporter mice are essentially PAPP-A knockouts (KO), which is how they are labeled in the text.

WT mice were treated with control (anti-TeTx, IgG$_1$) or anti-PAPPA antibody (IgG$_1$) at 10 mg/kg via IP injection once a week for the duration of each study.

4.6 | Preparation of tissues and isolation of cells by flow cytometry

Hematopoietic stem and progenitor cells (HSPCs) were analyzed and/or sorted as described (Mohrin et al., 2010, 2015). To obtain bone marrow cells, mice were sacrificed via CO_2 asphyxiation followed by cervical dislocation. For bone marrow analysis, mice were analyzed one at a time and only leg bones were used (2 femur and 2 tibia per mouse). For bone marrow sorting, groups of 5 mice were pooled and all major bones were used (2 femur, 2 tibia, 2 ilium, 2 humerus, 2 radius, 2 ulna per mouse). Bone marrow cells were harvested in staining media (SM) (PBS without Ca^{2+} or Mg^{2+} supplemented with 2% fetal bovine serum) by gently crushing bones with a mortar and pestle and filtering through 40-um cell strainers. Erythrocytes were lysed in ACK (150 mM NH4Cl/10 mM KHCO3) lysis buffer, and then, remaining cells were washed in SM. Bone marrow cells were counted using a Vi-Cell and then aliquoted for staining for FACS. For sorting, bone marrow cells were purified on a Ficoll gradient (Histopaque 1119, Sigma-Aldrich, #11191-100 ml) to remove bone dust and dying cells. Cells were then enriched for HSPCs by using c-Kit microbeads (Miltenyi Biotec, #130-091–224) and MACS Separation LS Columns (Miltenyi Biotec, #130-042–401).

Blood was collected via retro-orbital bleed or via terminal cardiac puncture and collected in EDTA-coated tubes (Becton Dickinson). Erythrocytes were lysed in ACK lysis buffer, and then, remaining cells were washed in SM. Blood cells were then stained for FACS analysis.

Spleens were dissociated by gently pressing spleen through a 40-um cell strainer with the plunger of a 3-ml syringe and washing with SM. Erythrocytes were lysed in ACK lysis buffer, and then, remaining cells were washed in SM. Spleen cells were counted using a Vi-Cell and then aliquoted for staining for FACS analysis.

To analyze or sort HSPCs, cells were stained with the following antibodies: biotinylated lineage markers [Mac-1 (CD11b), Gr-1 (Ly-6G/C), Ter119 (Ly76), CD3, CD4, CD5, CD8a (Ly-2), and B220 (CD45R) (BioLegend)] and streptavidin-conjugated BUV-395, IL7Ra (CD127) BUV-737, FCgR BV-711, CD48 BV-605, Flk2 (CD135) BV-421, Sca-1 (Ly-6A/E) PE-Cy7, CD150 PE-594, CD34 PE, C-kit APC-Cy7. To analyze or sort mature immune cells, cells were stained with the following antibodies: CD11b BUV-737, B220 BUV-496, F4/80 BV-650, Gr1 BV-421, CD3 PE. To analyze or sort MSCs, bone marrow cells were stained with the following antibodies: CD45 BUV-395, CD31 BUV-395, Ter119 BUV-395, CD140a APC, Biotinylated LepR, and Streptavidin PE.

MSCs were isolated similarly as described (Baryawno et al., 2019; Decker et al., 2017; Vanlandewijck et al., 2018; Zhou et al., 2014). Bones were crushed using a mortar and pestle in SM. Both marrow and bone fragments were then dissociated in 1 mg/ml STEMxyme (Worthington, #LS004106), 1 mg/ml Dispase II (Thermo Fisher Scientific, #17105041), and DNAseI (200U/ml, Roche, #10104159001) in SM at 37°C for 25 minutes shaking. Cells were then filtered sequentially through 110-um and 70-um cell strainers, and washed, and then, erythrocytes were lysed using ACK lysis buffer. Cells were then labeled with Dynabead-conjugated antibodies that had been prepared the night before. To prepare antibody-Dynabead conjugates, 200ul Sheep Anti-Rat IgG Dynabeads (Thermo Fisher Scientific, #11035) per mouse were incubated overnight at 4°C shaking with Rat anti-mouse antibodies against CD45, CD31, Ter119, B220, CD3, CD4, CD5, CD8, Gr1, and CD11b. The next day, just before adding prepared cells, tubes were put on Dyna5 magnet (Thermo Fisher Scientific, #12303D) and the supernatant poured off. Then, prepared cells were added to the antibody-Dynabead conjugates (no longer on the magnet) and incubated at 4°C shaking for 45 minutes. Tubes were then put back on the Dyna5 magnet, and the negative fraction was collected. The cells from the negative fraction were then stained with CD45-BUV395, CD31-BUV395, Ter119-BUV395, CD140a-APC, Biotinylated LepR, and Streptavidin PE, and MSCs were sorted.

Flow cytometry analysis was performed on a BD Fortessa, and flow cytometry cell sorting was performed on a BD FACS ARIA. All data analysis was done using BD Diva and Treestar FlowJo software programs.

HSC markers: Lin(–), c-Kit (+), Sca-1(+), CD48(–), CD150(+)
CMP markers: Lin(–), c-Kit (+), Sca- 1(–), FCgR(–), CD34(+)
CLP markers: Lin(–), Flk2(+), IL7Ra(+)
MEP markers: Lin(–), c-Kit (+), Sca- 1(–), FCgR(–), CD34(–)
GMP markers: Lin(–), c- Kit (+), Sca-1(–), FCgR(+), CD34(+)
MSC markers: CD31(–), CD45(–), Ter119(–), PDGFRa/CD140a(+), LepR(+)
B-cell markers: B220(+)
T-cell markers: CD3(+)
Myeloid markers: CD11B(+)

Detailed list of antibodies used for flow cytometry:

Cell type	Antigen	Conjugate	Company	Catalog #	Clone
HSPC	B220/CD45R	Biotin	BioLegend	103204	RA3-6B2
	CD3e	Biotin	BioLegend	100304	145-2C11
	CD4	Biotin	BioLegend	100404	GK1.5
	CD5	Biotin	BioLegend	100604	53–7.3
	CD8	Biotin	BioLegend	100704	53–6.7
	Mac1/CD11b	Biotin	BioLegend	101204	M1/70
	Gr1/Ly6G-Ly6C	Biotin	BioLegend	108404	RB6-8C5
	Ter119	Biotin	BioLegend	116204	TER–119
	Streptavidin	BUV395	BD	564176	n/a
	IL7Ra/CD127	BUV737	BD	564399	SB/199
	FCGR/CD16/32	BV711	BioLegend	101337	93
	CD48	BV605	BioLegend	103441	HM48-1
	Flk2/CD135	BV421	BD	562898	A2F10.1
	Sca1/Ly6A/E	PECy7	BioLegend	108114	D7
	CD150	PE594	BioLegend	115936	TC15-12F12.2
	CD34	PE	BioLegend	551387	RAM34
	C-kit/CD117	APCCy7	BioLegend	105826	2B8
MATURE	Mac1/CD11b	BUV737	BD	564443	M1/70
	B220/CD45R	BUV496	BD	564662	RA3-6B2
	Gr1/Ly6G-Ly6C	BV421	BioLegend	108434	RB6-8C5
	CD3e	PE	BioLegend	100308	145-2C11
	F4/80	BV605	BioLegend	123149	BM8
MSC	CD31	BUV395	BD	740239	390
	CD45	BUV395	BD	564279	30-F11
	Ter119	BUV395	BD	563827	TER–119
	CD140a/PDGFRa	APC	BioLegend	135908	APA5
	LepR	Biotin	R&D	BAF497	BAF497
	Streptavidin	PE	eBiosciences	12–4317–87	n/a
	CD31	Purified Rat anti-mouse	BioLegend	102502	MEC13.3
	CD45	Purified Rat anti-mouse	BioLegend	103102	30-F11
	Ter119	Purified Rat anti-mouse	BioLegend	116202	TER–119
	B220	Purified Rat anti-mouse	BioLegend	103202	RA3-6B2
	CD3	Purified Rat anti-mouse	BioLegend	100202	17A2
	CD4	Purified Rat anti-mouse	BioLegend	100402	GK1.5
	CD5	Purified Rat anti-mouse	BioLegend	100602	53–7.3
	CD8	Purified Rat anti-mouse	BioLegend	100702	53–6.7
	Gr1	Purified Rat anti-mouse	BioLegend	108402	RB6-8C5
	CD11B	Purified Rat anti-mouse	BioLegend	101202	M1/70

4.7 | Osteogenesis assay

Freshly isolated primary mouse MSCs were plated at a density of 5,000 cells/cm^2 on collagen-coated (5 µg/cm^2, Collagen I, Thermo Fisher Scientific, cat# A1048301) glass plates and cultured under normal conditions in Mesenchymal Stem Cell Growth Medium (MSCGM™, Lonza Walkersville, MD, cat# PT-3001) for 2 days. Medium was then changed to StemPro™ Osteogenesis Differentiation medium (Thermo Fisher Scientific, cat# A1007201) for differentiation wells or kept as MSCGM for control wells. Medium was replaced every 3–4 days for 17 days. To assess osteogenic differentiation, cells were fixed and stained using OsteoImage™ Mineralization assay (Lonza Walkersville, MD, cat# PA-1503) following the manufacturer instructions.

4.8 | Gene expression

IMR-90 human lung fibroblasts (ATCC CCL-186), HeLa human cervical epithelial cells (ATCC CRM-CCL-2), and 293 T human embryonic kidney epithelial cells (ATCC CRL-3216) cell lines were procured from ATCC and cultured as recommended by ATCC. HeLa cells were plated in 10% serum-containing media, allowed to adhere overnight, then the next day were switched to serum-free medium for 24 hrs. Cells were then treated with one or a combination of the following recombinant proteins in serum-free media [recombinant human IGF-1 (Gibco#PHG0071), recombinant human IGFBP-4 (R&D #804-GB), and recombinant human PAPP-A (R&D #2487-ZN (aa 82–1627 full length)] at the ratio of 5 nM: 20 nM: 2 nM (IGF-I: IGFBP-4: PAPP-A) for 60 minutes. Cells were then washed, and RNA was collected using TRIzol.

RNA was extracted from whole tissues using the Qiagen RNeasy 96 Universal Tissue Kit (Qiagen, 74881) and was digested with DNAseI before preparation for RNA-seq. RNA was extracted from low numbers of sorted populations using TRIzol reagent (Invitrogen), and Linear Acrylamide (Thermo Fisher, #AM9520) was used to aid precipitation and pellet visualization; RNA was then digested with DNaseI before preparation for RNA-seq.

Sequencing libraries were prepared as directed using either TruSeq® Stranded Total RNA Library Prep Human/Mouse/Rat (Illumina) or NEBNext® Ultra™ II Directional RNA Library Prep Kit (NEB). Samples were amplified for 10–13 cycles and sequencing on a HiSeq 4000 (Illumina). Sequencing quality control was performed using FastQC (v0.11.5). Transcript expression was then quantified using Salmon (v0.9.1) (Patro et al., 2017) in pseudo-alignment mode, without adapter trimming, producing per-gene count estimates, using the Ensembl mm10 transcriptome. Normalized count and differential expression analysis were performed in R using DESeq2 (v1.22.2) (Love et al., 2014), with a pseudo-count of 0.5 added to all normalized counts. For the cross-tissue analysis in Figure 1, treatment effect was extracted from a model incorporating sex and tissue as covariates (value ~sex + treatment +tissue).

4.9 | Bone analyses

4.9.1 | Micro-computed tomography (µCT)

High-resolution micro-computed tomographic imaging (µCT40, Scanco Medical AG, Brüttiselen, Switzerland) was used to assess microarchitecture and mineral density in the femur and fifth lumber (L5) vertebra of each mouse. In the femur, trabecular bone microarchitecture and cortical bone morphology were measured in the distal femoral metaphysis and mid-diaphysis, respectively. Trabecular bone was analyzed in the L5 vertebral body. Scans were acquired using a 10 μm^3 isotropic voxel size, 70 kVP peak X-ray tube potential, 114 mAs tube current, 200-ms

integration time, and were subjected to Gaussian filtration and segmentation. Image acquisition and analysis protocols adhered to the JBMR guidelines for the assessment of rodent bones by µCT (Bouxsein et al., 2010). In the distal femur, trabecular bone was evaluated in a region of interest beginning 200 µm superior to the distal growth plate and extending proximally 1500 µm (150 slices). Trabecular bone in the L5 vertebral body was analyzed in a region that extended from 100 µm inferior to the cranial endplate to 100 µm superior to the caudal end plate. Images were thresholded using an adaptive-iterative thresholding algorithm. The average adaptive-iterative threshold of the female Control mice (375 $mgHA/cm^3$) was then used as the threshold to segment bone from soft tissue in all samples, and the Scanco trabecular bone morphometry script was used to measure trabecular bone volume fraction (Tb.BV/TV, %), trabecular bone mineral density (Tb.BMD, $mgHA/cm^3$), trabecular-specific bone surface (Tb.BS/BV, mm^2/mm^3), trabecular thickness (Tb.Th, mm), trabecular number (Tb.N, mm^{-1}), trabecular separation (Tb.Sp, mm), and connectivity density (ConnD, $1/mm^3$). Cortical bone was assessed in 50 transverse µCT slices (500 µm long region) at the femoral mid-diaphysis, and the region included the entire outermost edge of the cortex. Cortical bone was segmented using a fixed threshold of 700 $mgHA/cm^3$. The following variables were computed the following: total cross-sectional area (bone +medullary area) (Tt.Ar, mm^2), cortical bone area (Ct.Ar, mm^2), medullary area (Ma.Ar, mm^2), bone area fraction (Ct.Ar/Tt.Ar, %), cortical tissue mineral density (Ct.TMD, $mgHA/cm^3$), cortical thickness (Ct.Th, mm), cortical porosity (%), and maximum, minimum, and polar moments of inertia (I_{max}, I_{min}, and J, mm^4).

4.9.2 | Mechanical Testing (Three-point bending)

Femurs were mechanically tested in three-point bending using a materials testing machine (Electroforce 3230, Bose Corporation, Eden Prairie, MN). The bending fixture had a bottom span length of 8 mm. The test was performed with the load point in displacement control moving at a rate of 0.05 mm/sec with force and displacement data collected at 60 Hz. All of the bones were positioned in the same orientation during testing with the cranial surface resting on the supports and being loaded in tension. Bending rigidity (EI, $N\text{-}mm^2$), apparent modulus of elasticity (E_{app}, MPa), ultimate moment (M_{ult}, N-mm), apparent ultimate stress (σ_{app}, MPa) work to fracture (W_{frac}, mJ), and apparent toughness (U_{app}, mJ/mm^3) were calculated based on the force and displacement data from the tests and the mid-shaft geometry measured with µCT. Work to fracture is the energy that is required to cause the femur to fracture, and it was calculated by finding the area under the force–displacement curve using the Riemann Sum method. Bending rigidity was calculated using the linear portion of the force-displacement curve. The minimum moment of inertia (I_{min}) was used when calculating the apparent modulus of elasticity.

4.9.3 | Dynamic histomorphometry

9 days prior to takedown, animals were injected with calcein (20 mg/kg, IP). 2 days prior to takedown, animals were injected with calcein +demeclocycline (10 mg/kg and 40 mg/kg, respectively, IP). Undecalcified vertebra and tibia bone samples were fixed and stored in 70% ethanol. Samples were embedded, then cut by IsoMet 1000 Precision Saw (Buehler, USA) to separate into proximal part of tibia for longitudinal tibia section and distal part of tibia for cortical tibia cross section. The separation is in the exact midpoint between superior tibiofibular joint and distal tibiofibular joint. The bone samples were dehydrated with acetone and embedded in methyl methacrylate. Consecutive sections were cut in 4 μm thickness by microtome (RM2255, Leica, Germany). Sections were stained with Von Kossa for showing the mineralized bone and 2% Toluidine Blue (pH3.7) for the analysis of osteoblast, osteoclast, and osteoid. The unstained sections were mounted with coverslip for dynamic parameters measurement. The bone sections were viewed with the Nikon E800 microscope equipped with Olympus DP71 digital camera. The image capture was performed by using Olympus CellSens software. The vertebra bone section histomorphometric data were obtained from under 200X magnification in a 1.3 mm x 1.8 mm region away from the growth plate. The tibia longitudinal bone section histomorphometric data were obtained from under 200X magnification in a 0.9 mm x 1.3 mm region away from the growth plate. The tibia cortical bone section histomorphometric data were obtained from under 100X magnification in a 2.6 mm x 1.8 mm region. OsteoMeasure analyzing software (OsteoMetrics Inc., Decatur, GA, USA) was used to generate and calculate the data. The structural parameters [bone volume (BV/TV), trabecular thickness (Tb.Th), and trabecular number (Tb.N), trabecular separation (Tb.Sp), cortical tissue area (Ct.T.Ar), cortical bone area (Ct.B.Ar), cortical marrow area (Ct.Ma.Ar), cortical bone volume (Ct.BV/TV), cortical thickness (Ct.Th), endocortical perimeter (Ec.Pm), and periosteal perimeter (Ps.Pm)] were obtained by taking an average of 2 different measurement from consecutive sections. The parameters were presented according to the standardized nomenclature (Dempster et al., 2013).

4.9.4 | Adiposity

Bone marrow adiposity was assessed in the proximal tibia for the presence of adipocyte "ghosts" under 200X magnification, using the same region of interest used to assess bone parameters. Adipose volume per tissue volume (Ad.V/TV) was calculated by OsteoMeasure analyzing software (OsteoMetrics Inc., Decatur, GA, USA). Adipocyte number (Ad.N) and tissue area (TA) were obtained from OsteoMeasure analyzing software (OsteoMetrics Inc., Decatur, GA, USA). Bone volume (BV) was determined as noted above.

4.10 | Statistical analysis

Unless noted otherwise (e.g., RNA-seq analysis), groups were compared using a Mann–Whitney U test (Wilcoxon rank-sum test). Where noted, multiple hypothesis testing was accounted for by determining FDR-adjusted q-values (Benjamini–Hochberg method). When sexes were analyzed together (p-combined), data were first analyzed for a significant sex difference in control animals. If a sex difference was not evident, sexes were simply pooled for treatment group analysis. If a sex difference in controls was detected, sex was accounted for in a linear model including an interaction term (value ~sex*treatment) and the treatment p-value was extracted. P-values for timecourses represent group:day interaction term in a linear mixed model (combined: value ~treatment*day +sex*treatment + (1|mouse); individual sexes: value ~treatment*day + (1|mouse). All error bars are standard deviation.

CONFLICT OF INTEREST
MM, JL, JZS, GK, GK, JP, KH, and AF are employees of Calico Life Sciences LLC. SB, JMT, AB, and YK are employees of AbbVie Inc. DH, DB, LA, MLB, and RB have no competing interests.

AUTHOR CONTRIBUTIONS
MM and AF conceptualized the study; MM, JL, SB, JMT, AB, GK, and YK contributed to methodology; MM, JL, JZS, DH, DB, GK, GK, LA, JP, and KH investigated the study; MLB, RB, YK, and AF involved in project administration; MM and AF wrote the manuscript; AF supervised the study.

DATA AVAILABILITY STATEMENT
All high-throughput sequencing data used in this study are available in NCBI GEO (http://www.ncbi.nlm.nih.gov/geo/), accession number GSE144618. anti-PAPP-A antibody and control antibody may be made available subject to a materials transfer agreement with Calico Life Sciences LLC.

ORCID
Mary Mohrin https://orcid.org/0000-0002-1341-7556
Justin Liu https://orcid.org/0000-0002-5338-6491
Jose Zavala-Solorio https://orcid.org/0000-0003-2025-2507
Sakshi Bhargava https://orcid.org/0000-0002-3837-1224
Georgios Koukos https://orcid.org/0000-0002-9470-0651

Lama Alabdulaaly https://orcid.org/0000-0002-9855-4321
Kayley Hake https://orcid.org/0000-0003-3310-1417
Mary L. Bouxsein https://orcid.org/0000-0002-7027-7414
Adam Freund https://orcid.org/0000-0002-7956-5332

REFERENCES

Bale, Laurie K., West, Sally A., & Conover, Cheryl A. (2017). Inducible knockdown of pregnancy-associated plasma protein-A gene expression in adult female mice extends life span. *Aging Cell*, *16*(4), 895–897. https://doi.org/10.1111/acel.12624

Barbieri, M., Bonafè, M., Franceschi, C., & Paolisso, G. (2003). Insulin/ IGF-I-signaling pathway: an evolutionarily conserved mechanism of longevity from yeast to humans. *American Journal of Physiology-Endocrinology and Metabolism*, *285*, E1064–E1071.

Baryawno, N., Przybylski, D., Kowalczyk, M. S., Kfoury, Y., Severe, N., Gustafsson, K., Kokkaliaris, K. D., Mercier, F., Tabaka, M., Hofree, M., Dionne, D., Papazian, A., Lee, D., Ashenberg, O., Subramanian, A., Vaishnav, E. D., Rozenblatt-Rosen, O., Regev, A., & Scadden, D. T. (2019). A cellular taxonomy of the bone marrow stroma in homeostasis and leukemia. *Cell*, *177*(7), 1915–1932.e16. https://doi.org/10.1016/j.cell.2019.04.040

Bayes-Genis, A., Schwartz, R. S., Lewis, D. A., Overgaard, M. T., Christiansen, M., Oxvig, C., Ashai, K., Holmes, D. R., & Conover, C. A. (2001). Insulin-like growth factor binding protein-4 protease produced by smooth muscle cells increases in the coronary artery after angioplasty. *Arteriosclerosis, Thrombosis, and Vascular Biology*, *21*, 335–341.

Becker, M. A., Haluska, P., Bale, L. K., Oxvig, C., & Conover, C. A. (2015). A novel neutralizing antibody targeting pregnancy-associated plasma protein-a inhibits ovarian cancer growth and ascites accumulation in patient mouse tumorgrafts. *Molecular Cancer Therapeutics*, *14*, 973–981.

Beckwith, H., & Yee, D. (2015). Minireview: Were the IGF signaling inhibitors all bad? *Molecular Endocrinology*, *29*, 1549–1557.

Boldt, H. B., Kjaer-Sorensen, K., Overgaard, M. T., Weyer, K., Poulsen, C. B., Sottrup-Jensen, L., Conover, C. A., Giudice, L. C., & Oxvig, C. (2004). The Lin12-notch repeats of pregnancy-associated plasma protein-A bind calcium and determine its proteolytic specificity. *Journal of Biological Chemistry*, *279*, 38525–38531.

Bouxsein, M. L., Boyd, S. K., Christiansen, B. A., Guldberg, R. E., Jepsen, K. J., & Müller, R. (2010). Guidelines for assessment of bone microstructure in rodents using micro–computed tomography. *Journal of Bone and Mineral Research*, *25*, 1468–1486.

Cawthorn, W. P., Scheller, E. L., & MacDougald, O. A. (2012). Adipose tissue stem cells meet preadipocyte commitment: going back to the future. *Journal of Lipid Research*, *53*, 227–246.

Chen, B.-K., Leiferman, K. M., Pittelkow, M. R., Overgaard, M. T., Oxvig, C., & Conover, C. A. (2003). Localization and regulation of pregnancy-associated plasma protein A expression in healing human skin. *Journal of Clinical Endocrinology and Metabolism*, *88*, 4465–4471.

Conover, C. A., & Bale, L. K. (2007). Loss of pregnancy-associated plasma protein A extends lifespan in mice. *Aging Cell*, *6*, 727–729.

Conover, C. A., Bale, L. K., Harrington, S. C., Resch, Z. T., Overgaard, M. T., & Oxvig, C. (2006). Cytokine stimulation of pregnancy-associated plasma protein A expression in human coronary artery smooth muscle cells: inhibition by resveratrol. *Am. J. Physiol.-cell Physiol.*, *290*, C183–C188.

Conover, C.A., Bale, L. K., Mader, J. R., Mason, M. A., Keenan, K. P., & Marler, R. J. (2010). Longevity and age-related pathology of mice deficient in pregnancy-associated plasma protein-A. *Journals of Gerontology. Series A, Biological Sciences and Medical Sciences*, *65*, 590–599.

Conover, C. A., Bale, L. K., & Oxvig, C. (2016). Targeted Inhibition of Pregnancy-Associated Plasma Protein-A Activity Reduces Atherosclerotic Plaque Burden in Mice. *J Cardiovasc Transl. Res.*

Conover, C. A., Chen, B.-K., & Resch, Z. T. (2004). Regulation of pregnancy-associated plasma protein-A expression in cultured human osteoblasts. *Bone*, *34*, 297–302.

Conover, C. A., Harstad, S. L., Tchkonia, T., & Kirkland, J. L. (2013). Preferential impact of pregnancy-associated plasma protein-A deficiency on visceral fat in mice on high-fat diet. *Am. J. Physiol. - Endocrinol. Metab.*, *305*, E1145–E1153.

Crisan, M., Yap, S., Casteilla, L., Chen, C.-W., Corselli, M., Park, T. S., Andriolo, G., Sun, B., Zheng, B. O., Zhang, L. I., Norotte, C., Teng, P.-N., Traas, J., Schugar, R., Deasy, B. M., Badylak, S., Bűhring, H.-J., Giacobino, J.-P., Lazzari, L., ... Péault, B. (2008). A Perivascular Origin for Mesenchymal Stem Cells in Multiple Human Organs. *Cell Stem Cell*, *3*, 301–313.

Crudden, C., Girnita, A., & Girnita, L. (2015). *Targeting the IGF-1R: The Tale of the Tortoise and the Hare* (p. 6). Front.

da Meirelles, L. da S., Chagastelles, P. C., & Nardi, N.B. (2006). Mesenchymal stem cells reside in virtually all post-natal organs and tissues. *Journal of Cell Science*, *119*, 2204–2213.

de Magalhaes, J. P., Curado, J., & Church, G. M. (2009). Meta-analysis of age-related gene expression profiles identifies common signatures of aging. *Bioinformatics*, *25*, 875–881.

Decker, M., Martinez-Morentin, L., Wang, G., Lee, Y., Liu, Q., Leslie, J., & Ding, L. (2017). Leptin-receptor-expressing bone marrow stromal cells are myofibroblasts in primary myelofibrosis. *Nature Cell Biology*, *19*, 677–688.

Dempster, D. W., Compston, J. E., Drezner, M. K., Glorieux, F. H., Kanis, J. A., Malluche, H., Meunier, P. J., Ott, S. M., Recker, R. R., & Parfitt, A. M. (2013). Standardized nomenclature, symbols, and units for bone histomorphometry: a 2012 update of the report of the ASBMR Histomorphometry Nomenclature Committee. *J. Bone Miner. Res. Off. J. Am. Soc. Bone Miner. Res.*, *28*, 2–17.

Ding, L., Saunders, T. L., Enikolopov, G., & Morrison, S. J. (2012). Endothelial and perivascular cells maintain haematopoietic stem cells. *Nature*, *481*, 457–462.

Dobnikar, L., Taylor, A. L., Chappell, J., Oldach, P., Harman, J. L., Oerton, E., Dzierzak, E., Bennett, M. R., Spivakov, M., & Jørgensen, H. F. (2018). Disease-relevant transcriptional signatures identified in individual smooth muscle cells from healthy mouse vessels. *Nature Communications*, *9*, 4567.

Duan, C., Hawes, S. B., Prevette, T., & Clemmons, D. R. (1996). Insulin-like Growth Factor-I (IGF-I) Regulates IGF-binding Protein-5 Synthesis through Transcriptional Activation of the Gene in Aortic Smooth Muscle Cells. *Journal of Biological Chemistry*, *271*, 4280–4288.

El Agha, E., Kramann, R., Schneider, R. K., Li, X., Seeger, W., Humphreys, B. D., & Bellusci, S. (2017). Mesenchymal Stem Cells in Fibrotic Disease. *Cell Stem Cell*, *21*, 166–177.

Fleming, J. M., Leibowitz, B. J., Kerr, D. E., & Cohick, W. S. (2005). IGF-I differentially regulates IGF-binding protein expression in primary mammary fibroblasts and epithelial cells. *Journal of Endocrinology*, *186*, 165–178.

Fontana, L., Partridge, L., & Longo, V. D. (2010). Extending Healthy Life Span—From Yeast to Humans. *Science*, *328*, 321–326.

Freese, K., Thasler, W.E., and Hellerbrand, C. (2016). Increased expression of pregnancy-associated plasma protein-A (PAPP-A) in hepatic stellate cells correlates with hepatic fibrosis and can be detected in the serum of patients with liver disease. In Zeitschrift Für Gastroenterologie, (Georg Thieme Verlag KG), p. A1.6.

Giladi, A., Paul, F., Herzog, Y., Lubling, Y., Weiner, A., Yofe, I., Jaitin, D., Cabezas-Wallscheid, N., Dress, R., Ginhoux, F., Trumpp, A., Tanay, A., & Amit, I. (2018). Single-cell characterization of haematopoietic progenitors and their trajectories in homeostasis and perturbed haematopoiesis. *Nature Cell Biology*, *20*, 836.

Gombos, A., Metzger-Filho, O., Dal Lago, L., & Awada-Hussein, A. (2012). Clinical development of insulin-like growth factor receptor—1 (IGF-1R) inhibitors: At the crossroad? Invest. *New Drugs*, *30*, 2433–2442.

Han, X., Wang, R., Zhou, Y., Fei, L., Sun, H., Lai, S., Saadatpour, A., Zhou, Z., Chen, H., Ye, F., Huang, D., Xu, Y., Huang, W., Jiang, M., Jiang, X., Mao, J., Chen, Y., Lu, C., Xie, J., … Guo, G. (2018). Mapping the Mouse Cell Atlas by Microwell-Seq. *Cell*, *172*, 1091–1107.e17.

Harrington, S. C., Simari, R. D., & Conover, C. A. (2007). Genetic deletion of pregnancy-associated plasma protein-A is associated with resistance to atherosclerotic lesion development in apolipoprotein E-deficient mice challenged with a high-fat diet. *Circulation Research*, *100*, 1696–1702.

Harstad, S. L., & Conover, C. A. (2014). Tissue-specific changes in pregnancy associated plasma protein-A expression with age in mice. *Experimental Gerontology*, *57*, 13–17.

He, L., Vanlandewijck, M., Mäe, M. A., Andrae, J., Ando, K., Del Gaudio, F., Nahar, K., Lebouvier, T., Laviña, B., Gouveia, L. et al (2018). Single-cell RNA sequencing of mouse brain and lung vascular and vessel-associated cell types. *Sci. Data*, *5*, 180160.

Heitzeneder, S., Sotillo, E., Shern, J. F., Sindiri, S., Xu, P., Jones, R., Pollak, M., Noer, P. R., Lorette, J., Fazli, L., Alag, A., Meltzer, P., Lau, C., Conover, C. A., Oxvig, C., Sorensen, P. H., Maris, J. M., Khan, J., & Mackall, C. L. (2019). *Pregnancy-Associated Plasma Protein-A (PAPP-A) in Ewing Sarcoma: Role in Tumor Growth and Immune Evasion. JNCI J. Natl.*

Hjortebjerg, R. (2018). IGFBP-4 and PAPP-A in normal physiology and disease. *Growth Horm. IGF Res.*, *41*, 7–22.

Jadlowiec, J., Dongell, D., Smith, J., Conover, C., & Campbell, P. (2005). Pregnancy-Associated Plasma Protein-A Is Involved in Matrix Mineralization of Human Adult Mesenchymal Stem Cells and Angiogenesis in the Chick Chorioallontoic Membrane. *Endocrinology*, *146*, 3765–3772.

Junnila, R. K., List, E. O., Berryman, D. E., Murrey, J. W., & Kopchick, J. J. (2013). The GH/IGF-1 axis in ageing and longevity. *Nat. Rev. Endocrinol.*, *9*, 366–376.

Kashyap, S., Hein, K. Z., Chini, C. C. S., Lika, J., Warner, G. M., Bale, L. K., Torres, V. E., Harris, P. C., Oxvig, C., Conover, C. A., & Chini, E. N. (2020). Metalloproteinase PAPP-A regulation of IGF-1 contributes to polycystic kidney disease pathogenesis. JCI. *Insight*.

Kenyon, C. J. (2010). The genetics of ageing. *Nature*, *464*, 504–512.

Kenyon, C., Chang, J., Gensch, E., Rudner, A., & Tabtiang, R. (1993). A C. elegans mutant that lives twice as long as wild type. *Nature*, *366*, 461–464.

Kfoury, Y., & Scadden, D. T. (2015). Mesenchymal Cell Contributions to the Stem Cell Niche. *Cell Stem Cell*, *16*, 239–253.

Kramann, R., Schneider, R. K., DiRocco, D. P., Machado, F., Fleig, S., Bondzie, P. A., Henderson, J. M., Ebert, B. L., & Humphreys, B. D. (2015). Perivascular Gli1+ Progenitors Are Key Contributors to Injury-Induced Organ Fibrosis. *Cell Stem Cell*, *16*, 51–66.

Kuemmerle, J. F. (2000). Endogenous IGF-I regulates IGF binding protein production in human intestinal smooth muscle cells. Am. J. Physiol.-Gastrointest. *Liver Physiol.*, *278*, G710–G717.

Laursen, L. S., Overgaard, M. T., Søe, R., Boldt, H. B., Sottrup-Jensen, L., Giudice, L. C., Conover, C. A., & Oxvig, C. (2001). Pregnancy-associated plasma protein-A (PAPP-A) cleaves insulin-like growth factor binding protein (IGFBP)-5 independent of IGF: implications for the mechanism of IGFBP-4 proteolysis by PAPP-A. *FEBS Letters*, *504*, 36–40.

Laursen, L. S., Overgaard, M. T., Weyer, K., Boldt, H. B., Ebbesen, P., Christiansen, M., Sottrup-Jensen, L., Giudice, L. C., & Oxvig, C. (2002). Cell Surface Targeting of Pregnancy-associated Plasma Protein A Proteolytic Activity REVERSIBLE ADHESION IS MEDIATED BY TWO NEIGHBORING SHORT CONSENSUS REPEATS. *Journal of Biological Chemistry*, *277*, 47225–47234.

Lawrence, J. B., Oxvig, C., Overgaard, M. T., Sottrup-Jensen, L., Gleich, G. J., Hays, L. G., Yates, J. R., & Conover, C. A. (1999). The insulin-like growth factor (IGF)-dependent IGF binding protein-4 protease secreted by human fibroblasts is pregnancy-associated plasma protein-A. *Proceedings of the National Academy of Sciences*, *96*, 3149–3153.

Loncar, G., & von Haehling, S. (2014). Elevated PAPP-A sets alarm bells ringing in patients with cardiac chest pain. *Expert Review of Cardiovascular Therapy*, *12*, 5–8.

Love, M. I., Huber, W., & Anders, S. (2014). Moderated estimation of fold change and dispersion for RNA-seq data with DESeq2. *Genome Biology*, *15*, 550.

Maxson, S., Lopez, E. A., Yoo, D., Danilkovitch-Miagkova, A., & LeRoux, M. A. (2012). Concise Review: Role of Mesenchymal Stem Cells in Wound Repair. *Stem Cells Translational Medicine*, *1*, 142–149.

Mikkelsen, J. H., Gyrup, C., Kristensen, P., Overgaard, M. T., Poulsen, C. B., Laursen, L. S., & Oxvig, C. (2008). Inhibition of the proteolytic activity of pregnancy-associated plasma protein-A by targeting substrate exosite binding. *Journal of Biological Chemistry*, *283*, 16772–16780.

Mikkelsen, J. H., Resch, Z. T., Kalra, B., Savjani, G., Kumar, A., Conover, C. A., & Oxvig, C. (2014). Indirect targeting of IGF receptor signaling in vivo by substrate-selective inhibition of PAPP-A proteolytic activity. *Oncotarget*, *5*, 1014–1025.

Miller, B. S., Bronk, J. T., Nishiyama, T., Yamagiwa, H., Srivastava, A., Bolander, M. E., & Conover, C. A. (2007). Pregnancy associated plasma protein-A is necessary for expeditious fracture healing in mice. *Journal of Endocrinology*, *192*, 505–513.

Mingjun, L., & Delphine, G. (2019). Smooth Muscle Cell Phenotypic Diversity. *Arteriosclerosis, Thrombosis, and Vascular Biology*, *39*, 1715–1723.

Mohrin, M., Bourke, E., Alexander, D., Warr, M. R., Barry-Holson, K., Le Beau, M. M., Morrison, C. G., & Passegué, E. (2010). Hematopoietic Stem Cell Quiescence Promotes Error-Prone DNA Repair and Mutagenesis. *Cell Stem Cell*, *7*, 174–185.

Mohrin, M., Shin, J., Liu, Y., Brown, K., Luo, H., Xi, Y., Haynes, C. M., & Chen, D. (2015). A mitochondrial UPR-mediated metabolic checkpoint regulates hematopoietic stem cell aging. *Science*, *347*, 1374–1377.

Monget, P., Mazerbourg, S., Delpuech, T., Maurel, M.-C., Manière, S., Zapf, J., Lalmanach, G., Oxvig, C., & Overgaard, M. T. (2003). Pregnancy-Associated Plasma Protein-A Is Involved in Insulin-Like Growth Factor Binding Protein-2 (IGFBP-2) Proteolytic Degradation in Bovine and Porcine Preovulatory Follicles: Identification of Cleavage Site and Characterization of IGFBP-2 Degradation. *Biology of Reproduction*, *68*, 77–86.

Nestorowa, S., Hamey, F. K., Pijuan Sala, B., Diamanti, E., Shepherd, M., Laurenti, E., Wilson, N. K., Kent, D. G., & Göttgens, B. (2016). A single-cell resolution map of mouse hematopoietic stem and progenitor cell differentiation. *Blood*, *128*, e20–e31.

Orkin, S. H., & Zon, L. I. (2008). Hematopoiesis: An Evolving Paradigm for Stem Cell Biology. *Cell*, *132*, 631–644.

Patro, R., Duggal, G., Love, M. I., Irizarry, R. A., & Kingsford, C. (2017). Salmon provides fast and bias-aware quantification of transcript expression. *Nature Methods*, *14*, 417–419.

Raudvere, U., Kolberg, L., Kuzmin, I., Arak, T., Adler, P., Peterson, H., & Vilo, J. (2019). g:Profiler: a web server for functional enrichment analysis and conversions of gene lists (2019 update). *Nucleic Acids Research*, *47*, W191–W198.

Resch, Z. T., Chen, B.-K., Bale, L. K., Oxvig, C., Overgaard, M. T., & Conover, C. A. (2004). Pregnancy-associated plasma protein a gene expression as a target of inflammatory cytokines. *Endocrinology*, *145*, 1124–1129.

Resch, Z. T., Simari, R. D., & Conover, C. A. (2006). Targeted Disruption of the Pregnancy-Associated Plasma Protein-A Gene Is Associated with Diminished Smooth Muscle Cell Response to Insulin-like Growth Factor-I and Resistance to Neointimal Hyperplasia after Vascular Injury. *Endocrinology*, *147*, 5634–5640.

Schafer, M. J., White, T. A., Iijima, K., Haak, A. J., Ligresti, G., Atkinson, E. J., Oberg, A. L., Birch, J., Salmonowicz, H., Zhu, Y. I., Mazula,

D. L., Brooks, R. W., Fuhrmann-Stroissnigg, H., Pirtskhalava, T., Prakash, Y. S., Tchkonia, T., Robbins, P. D., Aubry, M. C., Passos, J. F., ... LeBrasseur, N. K. (2017). Cellular senescence mediates fibrotic pulmonary disease. *Nature Communications*, 8, 14532.

Schaum, N., Lehallier, B., Hahn, O., Pálovics, R., Hosseinzadeh, S., Lee, S. E., Sit, R., Lee, D. P., Losada, P. M., Zardeneta, M. E., Fehlmann, T., Webber, J. T., McGeever, A., Calcuttawala, K., Zhang, H., Berdnik, D., Mathur, V., Tan, W., Zee, A., ... Wyss-Coray, T. (2020). Ageing hallmarks exhibit organ-specific temporal signatures. *Nature*, 1–7.

Segerstolpe, Å., Palasantza, A., Eliasson, P., Andersson, E.-M., Andréasson, A.-C., Sun, X., Picelli, S., Sabirsh, A., Clausen, M., Bjursell, M. K., Smith, D. M., Kasper, M., Ämmälä, C., & Sandberg, R. (2016). Single-Cell Transcriptome Profiling of Human Pancreatic Islets in Health and Type 2 Diabetes. *Cell Metabolism*, 24, 593–607.

Shi, Y., He, G., Lee, W.-C., McKenzie, J. A., Silva, M. J., & Long, F. (2017). Gli1 identifies osteogenic progenitors for bone formation and fracture repair. *Nature Communications*, 8, 2043.

Slocum, E., Craig, A., Villanueva, A., & Germain, D. (2019). Parity predisposes breasts to the oncogenic action of PAPP-A and activation of the collagen receptor DDR2. *Breast Cancer Research*, 21, 56.

Sprenger, C. C., Plymate, S. R., & Reed, M. J. (2010). Aging-related alterations in the extracellular matrix modulate the microenvironment and influence tumor progression. *International Journal of Cancer*, 127, 2739–2748.

Suryawanshi, H., Morozov, P., Straus, A., Sahasrabudhe, N., Max, K. E. A., Garzia, A., Kustagi, M., Tuschl, T., & Williams, Z. (2018). A single-cell survey of the human first-trimester placenta and decidua. *Sci. Adv.*, 4, eaau4788.

Swindell, W. R., Masternak, M. M., & Bartke, A. (2010). In vivo analysis of gene expression in long-lived mice lacking the pregnancy-associated plasma protein A (PappA) gene. *Experimental Gerontology*, 45, 366–374.

Tanner, S. J., Hefferan, T. E., Rosen, C. J., & Conover, C. A. (2008). Impact of Pregnancy-Associated Plasma Protein-A Deletion on the Adult Murine Skeleton. *Journal of Bone and Mineral Research*, 23, 655–662.

The Tabula Muris Consortium (2018). Single-cell transcriptomics of 20 mouse organs creates a Tabula Muris. *Nature*, 562, 367–372.

Tikhonova, A. N., Dolgalev, I., Hu, H., Sivaraj, K. K., Hoxha, E., Cuesta-Domínguez, Á., Pinho, S., Akhmetzyanova, I., Gao, J., Witkowski, M., Guillamot, M., Gutkin, M. C., Zhang, Y., Marier, C., Diefenbach, C., Kousteni, S., Heguy, A., Zhong, H., Fooksman, D. R., ... Aifantis, I. (2019). The bone marrow microenvironment at single-cell resolution. *Nature*, 1.

Torres, D., Hou, X., Bale, L., Heinzen, E. P., Maurer, M. J., Zanfagnin, V., Oberg, A. L., Conover, C., & Weroha, S. J. (2019). Overcoming platinum resistance in ovarian cancer by targeting pregnancy-associated plasma protein-A. *PLoS One*, 14, e0224564.

Vallejo, A. N., Michel, J. J., Bale, L. K., Lemster, B. H., Borghesi, L., & Conover, C. A. (2009). Resistance to age-dependent thymic atrophy in long-lived mice that are deficient in pregnancy-associated plasma protein A. *Proceedings of the National Academy of Sciences*, 106, 11252–11257.

Vanlandewijck, M., He, L., Mäe, M. A., Andrae, J., Ando, K., Del Gaudio, F., Nahar, K., Lebouvier, T., Laviña, B., Gouveia, L., Sun, Y., Raschperger, E., Räsänen, M., Zarb, Y., Mochizuki, N., Keller, A., Lendahl, U., & Betsholtz, C. (2018). A molecular atlas of cell types and zonation in the brain vasculature. *Nature*, 554, 475–480.

Veldhuis-Vlug, A. G., & Rosen, C. J. (2018). Clinical Implications of Bone Marrow Adiposity. *Journal of Internal Medicine*, 283, 121–139.

Weitzmann, M. N., Roser-Page, S., Vikulina, T., Weiss, D., Hao, L. I., Baldwin, W. H., Yu, K., del Mazo Arbona, N., McGee-Lawrence, M. E., Meeks, S. L., & Kempton, C. L. (2019). Reduced bone formation in males and increased bone resorption in females drive bone loss in hemophilia A mice. *Blood Adv.*, 3, 288–300.

Wenzel, S. E., & Balzar, S. (2006). Myofibroblast or Smooth Muscle. *American Journal of Respiratory and Critical Care Medicine*, 174, 364–365.

Weyer, K., Boldt, H. B., Poulsen, C. B., Kjaer-Sorensen, K., Gyrup, C., & Oxvig, C. (2007). A Substrate Specificity-determining Unit of Three Lin12-Notch Repeat Modules Is Formed in Trans within the Pappalysin-1 Dimer and Requires a Sequence Stretch C-terminal to the Third Module. *Journal of Biological Chemistry*, 282, 10988–10999.

Wirka, R. C., Wagh, D., Paik, D. T., Pjanic, M., Nguyen, T., Miller, C. L., Kundu, R., Nagao, M., Coller, J., Koyano, T. K., Fong, R., Woo, Y. J., Liu, B., Montgomery, S. B., Wu, J. C., Zhu, K., Chang, R., Alamprese, M., Tallquist, M. D., ... Quertermous, T. (2019). Atheroprotective roles of smooth muscle cell phenotypic modulation and the TCF21 disease gene as revealed by single-cell analysis. *Nature Medicine*, 25, 1280–1289.

Ye, P., & D'Ercole, J. (1998). Insulin-Like Growth Factor I (IGF-I) Regulates IGF Binding Protein-5 Gene Expression in the Brain. *Endocrinology*, 139, 65–71.

Zhou, B. O., Yue, R., Murphy, M. M., Peyer, J. G., & Morrison, S. J. (2014). Leptin-Receptor-Expressing Mesenchymal Stromal Cells Represent the Main Source of Bone Formed by Adult Bone Marrow. *Cell Stem Cell*, 15, 154–168.

Zhou, Y., Sun, B., Li, W., Zhou, J., Gao, F., Wang, X., Cai, M., & Sun, Z. (2019). *Pancreatic Stellate Cells: A Rising Translational Physiology Star as a Potential Stem Cell Type for Beta Cell Neogenesis* (p. 10). Front.

SUPPORTING INFORMATION

Additional supporting information may be found online in the Supporting Information section.